Master of Science Thesis
HT2020

Preparations for photon external beam radiotherapy treatment planning of small animals

Joanie Diha Guei

Supervisors

Crister Ceberg, Elise Konradsson and Johan Gustafsson

Medical Radiation Physics, Lund
Faculty of Science
Lund University
www.msf.lu.se

Acknowledgements

I am grateful to Crister Ceberg **(Professor, Medical Radiation Physics, Lund University)** for giving me a clear description of the XenX system and helping me with the comparison of the Monte Carlo dose calculations with radiochromic film measurements.

I want to address my deepest gratitude to Elise Konradsson **(Doctoral student, Medical Radiation Physics, Lund University)** for suggesting good literature about cone-beam computed tomography, small animal external beam radiotherapy, and for assisting me during the radiochromic film measurements.

I am also very grateful to Johan Gustafsson **(Researcher, Medical Radiation Physics, Lund University)** for helping me with the programming issues I encountered during this thesis.

I want to express my sincere gratitude to the Department of Medical Radiation Physics at Lund University for allowing me to do my thesis on the XenX.

Finally, I want to thank my family and my best friend for believing in me and supporting me during all six years of my education.

Förberedelser inför planering av extern strålbehandling av smådjur

Extern strålbehandling är en av den viktigaste typen av cancerbehandlingar och administreras till patienter genom användning av en strålbehandlingsapparat som kallas för linjäraccelerator. Linjäracceleratorn producerar bromsstrålning som används för att bota cancern.

För att säkerställa att behandlingen levereras med hög noggrannhet planeras den innan start. Ett viktigt steg i planeringen är beräkning av den absorberade dosen. Den absorberade dosen är mängden energi som deponeras per massenhet. Den absorberade dosen måste beräknas med så hög precision som möjligt för att bota cancern och samtidigt minimera biverkningar från behandlingen. Beräkningen av den absorberade dosen utförs i ett datorprogram som kallas för dosplaneringssystem och baseras på så kallade snittbilder av behandlingsområdet. Behandlingsområdet består av cancern och omkringliggande frisk vävnad. Information om hur strålningen påverkar dessa vävnader kan fås från prekliniska studier som ofta utförs på smådjur och sedan testas på människor innan kliniskt bruk. För att få värdefullt resultat från prekliniska studier är det viktigt att planering av prekliniska studierna efterliknar proceduren vid klinisk extern strålbehandling.

I detta arbete har realistiska mätfantom använts för att optimera bildtagning och utvärdera noggrannheten av ett dosplaneringssystem som används för att beräkna den absorberade dosen som ska ges till smådjur under prekliniska studier. Optimering av biltagningen har gått ut på att generera snittbilder som kan används för sådana beräkningar. Vidare, har noggrannheten i den beräknade absorberade dosen utvärderats genom jämförelse med mätningar. Den dedikerade prekliniska strålbehandlingsapparaten XenX har använts i arbetet.

Detta arbete har visat hur bildtagningen som används för planering av prekliniska studier på smådjur kan optimeras för att få snittbilder med mindre artefakter, mindre brus och högre upplösning. I arbetet har det också visats att för en noggrann beräkning av den absorberade dosen krävs att dosplanneringsystem förses med snittbilder som innehåller så lite artefakter och brus som möjligt.

Abstract

Introduction: The XenX is a small animal irradiation system that acquires high-resolution cone-beam tomography (CBCT) images of small animals and treats small animals with higher precision than medical linear accelerators. MuriSlice is a software for CBCT image reconstruction. This thesis aims to optimise the CBCT image reconstruction protocol in MuriSlice to enable the segmentation of CBCT images in the μRayStation 8B treatment planning system. In addition, the calculation of absorbed dose performed by the Monte Carlo dose calculation algorithm in μRayStation 8B based on the reconstructed CBCT images is verified by comparison with radiochromic film measurements.

Materials and methods: In the first part of this thesis, the XenX's integrated CBCT was used to acquire a set of projections of a cylindrical water phantom, a 3D printed mouse phantom, and a flat field. The acquired projections were used to optimise selected parameters of MuriSlice. First, the voxel size was selected based on the observed signal-to-noise ratio (SNR) in axial images of the cylindrical water phantom and recommendations of voxel size for CT imaging of small animals. Second, three corrections were performed on each projection, including 1) a correction for a distortion introduced by the lens in the digital camera of the CBCT imaging system, 2) a pixel-by-pixel correction to reduce the noise in the individual pixel of the flat field projections, and 3) a ring artefacts reduction using a 2D Butterworth filter. Third, the corrected projections were filtered with different pre-filters for further noise reduction. A pre-filter was selected based on the SNR and the contrast between soft tissue and bone in a transverse slice of the reconstructed images of the 3D printed mouse phantom. In the second part of this thesis, absorbed dose comparisons were carried out in four different slab phantoms containing various combinations of polystyrene, aluminium, and cork. Each phantom was irradiated by a 220 kV circular beam of X-ray photons (Ø = 10 mm). A set of CBCT projections for each slab phantom was acquired, reconstructed with the optimised protocol, and imported into μRayStation 8B. Inside μRayStation 8B, the reconstructed images of the slab phantoms were segmented into regions with the material composition assigned either based on the CBCT's Hounsfield unit to mass density calibration or by manual identification. The absorbed dose to the assigned material in the CBCT image of each slab phantom was estimated using the Monte Carlo dose calculation algorithm in μRayStation 8B and then compared with radiochromic film measurements.

Results: The reconstruction protocol in Murislice included a voxel size of $(100\,\mu m)^3$ and a edge-preserving denoising pre-filter. The optimisation of the reconstruction parameters resulted in a significant reduction of noise and near elimination of ring artefacts in the reconstructed image of the 3D printed mouse phantom. Furthermore, the contrast between the structures in the reconstructed CBCT image of the slab phantoms was sufficient to allow for the segmentation of relevant structures in the slab phantoms. The remaining noise resulted in a large fluctuation in estimated absorbed doses when the reconstructed images of the slab phantoms were segmented into regions with the assignment of the material composition based on the CBCT Hounsfield unit to mass density calibration. With the manual assignment of the material composition, the uncertainty in the estimated absorbed dose was within 1 %. The absorbed dose that was estimated with μRayStation 8B based on manual material assignment to the CBCT images of the slab phantoms was in reasonably good agreement with the film measurements, with a mean (max) of absolute difference in the percentage depth dose of 0.4 % (2.4%), 1.6% (2.9%), 3.5% (4.2%) and 4.6% (12%) with increasing complexity of the heterogeneity in the slab phantoms.

Conclusion: An optimised image reconstruction protocol for the XenX's built-in CBCT has been developed in MuriSlice. This image reconstruction protocol enables the reconstruction of CBCT images with reduced noise and a minimal number of ring artefacts. Future work is required to optimise additional reconstruction parameters for further noise reduction and less fluctuation in the absorbed dose calculations based on the CBCT images done using the μRayStation 8B.

Abbreviations

Abbreviation	Meaning
1D	One dimensional
2D	Two dimensional
3D	Three dimensional
AL	Aluminium
CBCT	Cone-beam computed tomography
CNR	Contrast-to-noise ratio(s)
CO	Cork
COD	Center of distortion
CT	Computed tomography
EBRT	External beam radiation therapy
HU	Hounsfield unit
FBP	Filtered back projection
FDK	FeldKamp, Devis and Kress
kV	Kilovotage
MC	Monte Carlo
MV	Megavoltage
NIST	National Institute of Standards and Technology
OAR	Organ(s) at risk
PDD	Percentage depth dose(s)
PS	Polystyrene
ROI	Region(s) of interest
SAEBRT	Small animal external beam radiotherapy
SAIGIS	Small animal image-guided irradiation system(s)
SNR	Signal-to-noise ratio(s)
TPS	Treatment planning system(s)

Contents

Chapter 1

Introduction

Cancer is among the leading causes of death worldwide [1]. In 2020, 18.1 million cancer cases were diagnosed worldwide [2]. Furthermore, half of the cancer patients in developed countries receive external beam radiotherapy (EBRT) as part of their treatment [3]. External beam radiotherapy is a form of cancer treatment that uses ionising radiation to eliminate cancerous cells [4]. The type of ionising radiation commonly employed in EBRT is a megavoltage (MV) beam of X-ray photons generated in medical linear accelerators [1]. The goal of EBRT is to deliver as high as possible absorbed dose (the term "dose" will be used hereafter) to the tumour while sparing the surrounding healthy tissues [1].

In small animal external radiotherapy (SAEBRT), small animals such as mice are used to investigate the response of normal tissues and tumours to EBRT or to a combination of EBRT and other types of cancer treatment such as immunotherapy and chemotherapy [5, 6]. The goal of the SAEBRT is to rapidly produce results that include data for normal tissue complication probability and tumor control probability for clinical trials, to provide benefits for the treatment of cancer patients [5]. Until the last decade, small animals were commonly treated using MV beams of X-ray photons and lead blocks [3, 5]. Furthermore, no commercial treatment planning system (TPS) for SAEBRT existed, and therefore individual treatment plans for the small animals could not be generated using such system during SAEBRT [3]. This simple treatment technique resulted in non-conformal dose delivery to the target in the small animals [5]. To generate results of good quality in SAEBRT for clinical trials, the dose delivery in SAEBRT must mimic the dose delivery of EBRT as much as possible, where X-ray computed tomography (CT) images are used for dose calculation and the prescribed dose is commonly delivered to the target with conformal treatment technique such as intensity-modulated radiotherapy [7]. To ensure conformal dose delivery in SAEBRT, several small animal image-guided irradiation systems (SAIGIS) have been developed in recent years [3]. The small animal irradiation systems generate kilovoltage (kV) beams of X-ray photons with field sizes as small as 1 mm in diameter [8], and are equipped with X-ray cone-beam computed tomography (CBCT) or CT imaging systems that can be used to acquire high-resolution 3D images of the small animals. The 3D images of the small animals can then be used in conjunction with a dose calculation algorithm available in the commercial TPS for SAEBRT that have also been developed during recent years for dose calculation [7]. The Monte Carlo (MC) dose calculation algorithm provides the most accurate estimation of the dose distributions for SAEBRT provided that the beam of kV X-ray photons from the SAIGIS and the small animal are modelled accurately [1, 7, 9, 10].

Our institution has acquired a SAIGIS called XenX (Xstrahl Ltd, Surrey, UK). The XenX is currently used for SAEBRT. The XenX has an indirect X-ray detector that is used to acquire 2D orthogonal images for verification of the small animal's positioning before treatment. In this thesis, the indirect X-ray detector was used to acquire CBCT images for dose calculations. MuriSlice (Xstrahl Ltd, Surrey, UK), a software for the reconstruction of CBCT images has also been acquired. The parameters for image reconstruction in MuriSlice needed to be optimised for dose calculation. Currently, the CBCT images of objects that are generated by MuriSlice contain several ring artefacts. Ring artefacts affect the dose calculations performed on CBCT images and therefore need to be reduced or removed completely from the reconstructed CBCT images to allow accurate dose calculation. Our institution also acquired μRayStation 8B (RaySearch Laboratories, Stockholm, Sweden), a TPS for SAEBRT. μRayStation 8B consists of an MC dose calculation algorithm that can be used in conjunction with CBCT images of small animals for dose calculation. An analytical model for a 220 kV beam of X-ray photons generated by the XenX for SAEBRT had been

created using the specification for the X-ray source provided by Xstrahl and validated by physical dose measurements. The analytical model of the kV beam of X-ray photons had been added to the μRayStation 8B to allow MC dose calculation for SAEBRT performed with the XenX.

1.1 Aim

This thesis aims:

1. to optimise the cone-beam computed tomography image reconstruction protocol in MuriSlice to enable segmentation of CBCT images in μRayStation 8B.
2. to verify the Monte Carlo dose algorithm in μRayStation 8B used for dose calculation on the reconstructed CBCT images by comparison with radiochromic film measurements.

Chapter 2

Background and theory

2.1 Description of the XenX system

The XenX system consists of the following essential components, an X-ray tube, a stage, a gantry, an indirect X-ray detector, and a collection of collimators. Figure 2.1 shows a photograph of the XenX system.

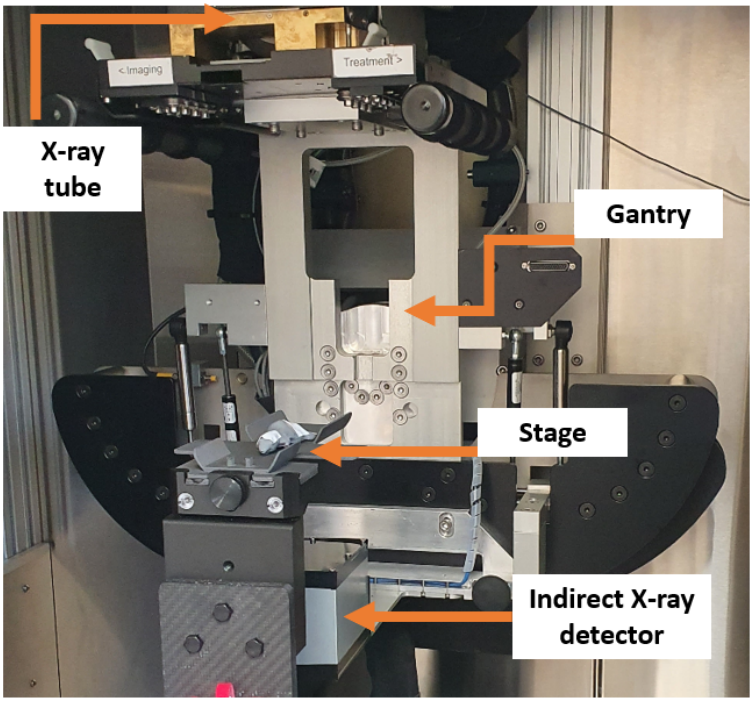

Figure 2.1: *Photograph of the XenX.*

The specifications of the X-ray tube can be found in Appendix A. CBCT imaging is done using 60 kV tube voltage and a 0.8 mA tube current with a 0.5 mm copper filter. For treatment, the XenX operates at 220 kV tube voltage and a 13 mA tube current with a 1.5 mm aluminium filter. The stage is controlled by a computer and can be translated in three directions (**Y**=*front and back*, **X**=*left and right*, and **Z**=*up and down*). The X-ray tube and indirect X-ray detector are mounted on the gantry which rotates around the stage during CBCT imaging. The indirect X-ray detector consists of a scintillator, a mirror and a digital camera (model: acA1920-50gm, Basler AG, Ahrensburg, Germany). The specifications of the digital camera are given in Appendix B. The small animals can be positioned at the isocenter

before CBCT imaging and treatment. To ensure conformal dose delivery during treatment, the kV beams of X-ray photons generated by the XenX are shaped to different field sizes by using different collimators including two fixed cylindrical collimators, three square collimators, a rectangular collimator, and a variable collimator. The collimators are described in table 2.1.

Table 2.1: *Description of the collimators.*

Collimator		**Value**
Cylindrical	diameter [mm]	5,10
Rectangular	width [mm] $\times$ Height [mm]	3×9
Square	side [mm]	3, 5, 10
Variable	maximum width [mm] $\times$ maximum height [mm]	40×80

The two fixed square and two cylindrical collimators are presented in figure 2.2a and 2.2b respectively. Figure 2.2c shows the XenX with a cylindrical collimator that was inserted in it.

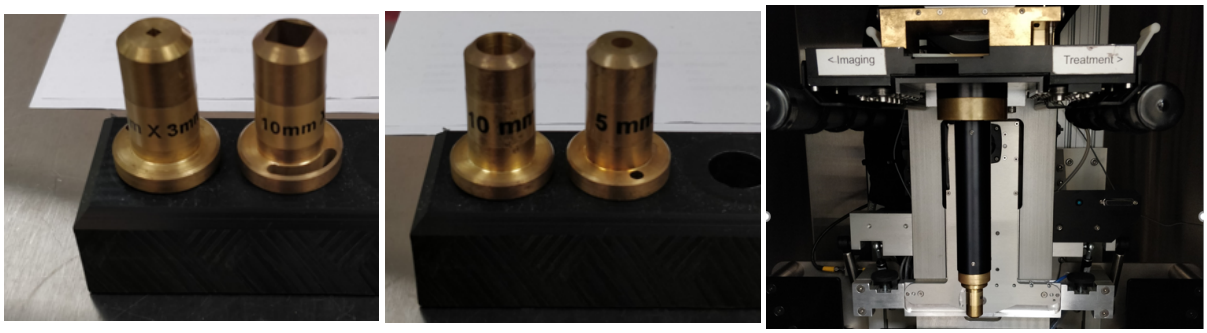

(a) (b) (c)

Figure 2.2: *Two square collimators (a), and two cylindrical collimators (b). One of these collimators that has been inserted in the XenX (c).*

2.2 X-ray photon-matter interactions and indirect X-ray detector

The X-ray tube of XenX can generate X-ray photons with energies ranging from 20 keV to 220 keV. In this energy range, the three following X-ray photon interaction processes dominate [1]: photoelectric absorption, Compton scattering, and Rayleigh scattering. During the photoelectric absorption, an incident X-ray photon transfers all its energy to a bound electron of absorbing matter. The electron leaves one of the atomic shells with a kinetic energy corresponding to the difference between the energy of the incident X-ray photon and the binding energy of the electron. After the electron leaves the atomic shell, the vacancy will be filled by an electron from one the other atomic shells, and Auger electrons or characteristic X-ray photons will be emitted [1]. The atomic cross-section for photoelectric absorption, ${}_{a}\tau$ is approximately proportional to [1]:

$$ {}_{a}\tau \propto \frac{Z^{n}}{hv^{3.5}}. \tag{2.1} $$

Where:

- Z: is the atomic number of the absorbing matter.
- n: is a constant which varies from 3 for low energy X-ray photons to 4.6 for high energy X-ray photons.
- hv: is the energy of the incident X-ray photon.

From Eq. 2.1, it is observed that the atomic cross-section for photoelectric absorption increases with decreasing X-ray photon energy and increasing high atomic number.

During Compton scattering, an incident X-ray photon collides with an electron of absorbing matter that is assumed to be free and at rest [1]. After the collision, the electron leaves the atom with a fraction of the energy of the incident X-ray photon [1]. During the collision, a scattered X-ray photon with energy smaller than the incident X-ray photon is produced [1]. The fraction of the energy that is distributed to both the free electron and the scattered X-ray photon after the collision depends on the scattering angle of the scattered X-ray photon, and the energy of the incident X-ray photon [1]. The atomic cross-section for Compton scattering, ${}_a\sigma_C$ is proportional to [1],

$$ {}_a\sigma_C \propto Z, \tag{2.2} $$

From Eq. 2.2 it is observed that the atomic cross-section for Compton scattering is proportional to the atomic number of the absorbing matter [1].

During the Rayleigh scattering process, an incident X-ray photon collides with the bound electrons of the absorbing matter and the incident X-ray photon changes direction while maintaining its initial energy after the collision [1, 11]. The atomic cross-section for Rayleigh scattering, ${}_a\sigma_R$ is proportional to [1],

$$ {}_a\sigma_R \propto \left(\frac{Z}{h\nu}\right)^2 \tag{2.3} $$

From Eq. 2.3 it is observed that the atomic cross-section for Rayleigh scattering increases with increasing atomic number of the absorbing matter and decreasing energy of the incident X-ray photon [1].

Indirect X-ray detectors are used in CBCT imaging systems to acquire cone-beam X-ray projections of the object for CBCT image reconstruction. Figure 2.3 shows a schematic representation of a typical indirect X-ray detector and illustrates its detection principle.

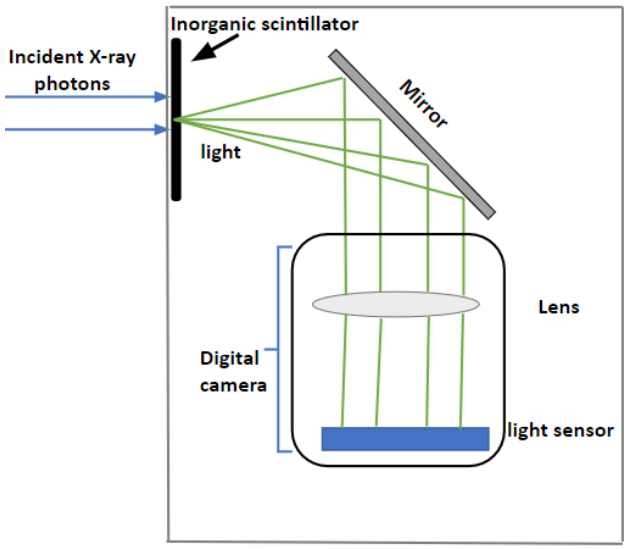

Figure 2.3: *Schematic representation of an indirect X-ray detector and illustration of its detection principle.*

The scintillator converts the incident X-ray photons into light. The scintillator layer consists of solid crystals [11], and the energy states of electrons in these crystals consist of a valence band and conduction band which are separated by an empty gap called bandgap [11]. When a X-ray photon enters the scintillator layer, it interacts with the atoms or molecules of the scintillator layer, and these interactions can result in the excitation of electrons from the valence band to the conduction band [12]. The excited electrons in the conduction band can emit visible light when they return to the valence band. Activators are impurities that are commonly added to the scintillator layer to introduce activator

energy states in the bandgap [12]. The space between the activator energy states is less than the space between the valence and conduction bands [12]. Light is emitted when the electrons in the conduction band return to the activator states [12]. The intensity of the light at a position in the scintillator layer is related to the intensity of the beam of X-ray photons that incident on the surface of the indirect X-ray detector at this position [13]. The light produced in the scintillator layer reaches the mirror which directs it into the digital camera. The lens in the digital camera focuses and directs the light into the light sensor in the digital camera. The light sensor consists of a large number of individual photodiode or pn-junction arranged in a two dimensional (2D) array. Each photodiode consists of a n-type and p-type silicon (see figure 2.4) [11, 14].

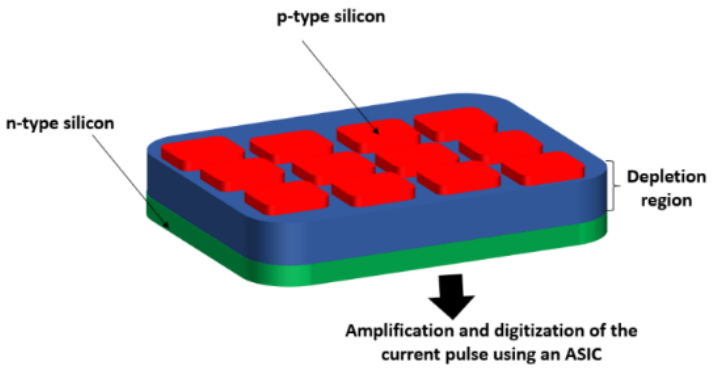

Figure 2.4: *The figure displays an example of a light sensor. Adapted from Roth [15].*

The n-type silicon has excess electrons while the p-type silicon crystal has excess holes [12]. A photodiode can be formed by combining the n-type silicon with the p-type silicon. Around the contact between the n-type and p-type silicon, a depletion region will be formed as the result of the recombination of electrons from the p-type silicon with the holes from the n-type silicon. The positively charged ions in the n-type silicon and negatively charged ions in the p-type silicon form an internal electric field within the depletion region. [12]. After the light is reflected by the mirror (see figure 2.4), it enters the depletion region where electron and hole pairs will be created [12]. The magnitude of the charge produced in each photodiode is proportional to the light emitted from the scintillator layer in the region around this photodiode. These charges form a current which is collected by an application-specific integrated circuit (ASCI). The ASCI amplifies and reads these charges [11, 13]. The read charges are then used to form the 2D X-ray projections of the object.

2.3 Basic principles of X-ray CT and CBCT

Assuming that an object is irradiated by a monoenergetic beam of X-ray photons with a certain energy, the intensity of the transmitted X-ray photons I(t) is given by the Beer-Lambert law [16],

$$I(t) = I(0)e^{-\int_t \mu(x,y)\,ds}. \tag{2.4}$$

Where:

- $I(0)$: is the intensity of the incident X-ray photons.
- $\mu(x,y)$: is the attenuation coefficient as function of position in the object.
- t: is the path length travelled by the X-ray photons in the object.

Two types of attenuation coefficients are the linear attenuation coefficient and mass attenuation coefficient. The linear attenuation coefficient is the sum of the cross-section for photoelectric absorption, Compton Scattering, and Rayleigh Scattering [11]. The linear attenuation coefficient depends on the energy of the incident X-ray photons,

the atomic number, and the density of the object [16]. The mass attenuation coefficient μ_m is related to the linear attenuation coefficient through,

$$\mu_m = \frac{\mu}{\rho} = \frac{1}{\rho}(_a\tau + _a\sigma_c + _a\sigma_R), \tag{2.5}$$

where ρ is the density of the object.

By rearranging Eq. 2.4 the following expression is obtained:

$$\int_t \mu(x,y)\,ds = -\ln\left(\frac{I(t)}{I(0)}\right). \tag{2.6}$$

Eq. 2.6 is a line integral of attenuation coefficients or X-ray projections and plays a central role in X-ray CT and CBCT.

2.4 X-ray CT and CBCT

Godfrey Newbold Hounsfield developed the first CT scanner in 1967 and showed that internal structures inside the body could be reconstructed from a set of X-ray measurements taken from different directions [17]. X-ray computed tomography is an imaging technique used to obtain cross-sectional images of the internal structures of an object [17]. X-ray computed tomography can be divided in two different steps,

1. Acquisition of one dimensional (1D) X-ray projections of the object.
2. 2D image reconstruction.

During the acquisition process, 1D X-ray projections are acquired using an X-ray source and an X-ray detector. Each 1D X-ray projection consists of a set of line integrals of attenuation coefficients [17, 16]. Two different geometries for the acquisition of 1D X-ray projections are presented in figure 2.5. These two geometries are referred to as parallel beam geometry (see figure 2.5a) and equispaced fan-beam geometry (see figure 2.5b)[16, 18]. In the parallel beam geometry, the 1D X-ray projections are acquired by rotating and translating an X-ray source emitting a pencil X-ray beam and an X-ray detector synchronously around the object [16]. In the equispaced fan-beam geometry, the 1D X-ray projections are acquired by rotating an X-ray source emitting a fan beam and a row of detectors around the object [18, 19].

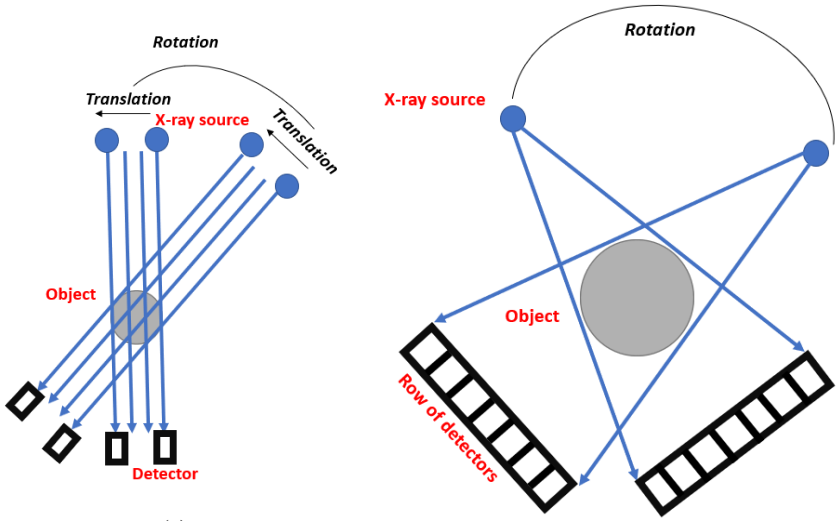

Figure 2.5: *Illustration of parallel beam acquisition geometry (a) and equispaced fan-beam acquisition geometry (b).*

During the 2D image reconstruction, the values of 1D X-ray projections are used as input in an image reconstruction algorithm to reconstruct cross-sectional images of the object. Filtered back projection (FBP) is the commonly most used reconstruction algorithm for the reconstruction of CT images [16]. The CT images represent the distribution of the attenuation coefficients inside the object [18].

Assume that $f(x,y)$ is the cross-sectional image to be reconstructed and that 1D X-ray projections from $f(x,y)$ are collected in the parallel beam acquisition geometry as shown in figure 2.6. Each straight line x' through $f(x,y)$ as shown in figure 2.6 can be described by [20],

$$x' = x\cos(\eta) + y\sin(\eta), \tag{2.7}$$

where:

- η: is a projection angle.
- x': is the coordinate of the detector.

A 1D X-ray projection $P(\eta, x')$ of $f(x,y)$ which is also known as its 2D radon transform $f(x,y)$ can be expressed as,

$$\mathscr{R}\{f(x,y)\} = P(\eta, x') = \int_{-\infty}^{\infty}\int_{-\infty}^{\infty} f(x,y)\,\delta(x\cos(\eta) + y\sin(\eta) - x')\,dx\,dy \tag{2.8}$$

where:

- $\mathscr{R}$: is the 2D radon transform operator.
- δ: is the Diract delta function.

The (x', y') coordinate system is the rotation of the (x,y) coordinate system [19]. Both coordinate systems are related through [18],

$$\begin{bmatrix} x' \\ y' \end{bmatrix} = \begin{bmatrix} \cos(\eta) & \sin(\eta) \\ -\sin(\eta) & \cos(\eta) \end{bmatrix} \begin{bmatrix} x \\ y \end{bmatrix} . \tag{2.9}$$

The radon transform of $f(x,y)$ is illustrated in figure 2.6.

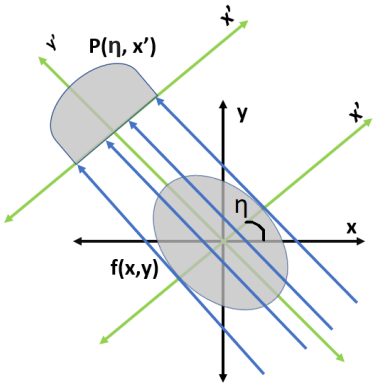

Figure 2.6: *Illustration of the 2D radon transform of* $f(x,y)$.

The values of the 1D X-ray projections are often visualised as an image in the η- x' coordinate system. Such representation of the values of the 1D X-ray projections is called a sinogram [16, 18].

An important theorem in the field of X-ray CT image reconstruction is the central slice theorem. The 2D central slice theorem states that the 1D Fourier transform of a 1D X-ray projection of $f(x,y)$ acquired at projection angle η is a profile through the 2D Fourier transform of $f(x,y)$ at the same angle [17]. Mathematically the 2D central slice theorem can be expressed as [17],

$$P(\eta, \tau) = F(\tau\cos(\eta), \tau\sin(\eta)). \tag{2.10}$$

Where

- $P(\eta,\tau)$: is the 1D Fourier transform of a projection $P(\eta,x')$.
- $F(\tau\cos(\eta),\tau\sin(\eta))$: is the 2D Fourier transform of the $f(x,y)$.
- τ: spatial frequency of $f(x,y)$.

The 1D Fourier transform of a projection $P(\eta,x')$ with respect to x' at a projection angle η can be expressed as [17]:

$$P(\tau,\eta)=\int_{-\infty}^{\infty}P(\eta,x')e^{-2\pi ix'\tau}d\tau. \tag{2.11}$$

Using the Fourier slice theorem, it can be shown that the mathematical expression of FBP for 1D X-ray projections acquired in the parallel beam acquisition geometry can be expressed as [17]:

$$f(x,y)=\int_0^{\pi}\left[\int_{-\infty}^{\infty}P(\eta,\tau)\cdot|\tau|\cdot e^{2\pi i\tau x'}d\tau\right]d\eta \tag{2.12}$$

where $|\tau|$ is the Ramachandran and Lakshminarayanan Ramp-Lak-filter.

In the inner integral of Eq. 2.12, it is observed that the Ramp-Lak-filter is multiplied by the Fourier transform of the 1D X-ray projections $P(\eta,\tau)$. If the Fourier transform of 1D X-ray projections contain noise, the noise will be amplified by the Ramp-Lak filter [21, 22]. Consequently, the reconstructed image $f(x,y)$ will be noisy [21, 22]. To reduce the noise level in the reconstructed image, the Fourier transform of the 1D X-ray projections are commonly multiplied by the Ramp-Lak-filter and a low pass filter [22]. From Eq. 2.12, it is observed that the Ramp-Lak-filter Eq. 2.12 has to be integrated over infinite number of spatial frequencies. In practice, the values of Fourier transform of the 1D X-ray projections are assume to be band-limited [17]. If the 1D X-ray projection values are sampled with the sampling interval Δx, then according to the Nyquist theorem the maximum frequency, ε in a sampled Fourier transform of a 1D X-ray projection must be [17],

$$\varepsilon=\frac{1}{2\Delta x}, \tag{2.13}$$

to avoid aliasing in the 1D X-ray projection and the reconstructed images [17].

Considering the limitations outlined in the previous paragraph, then Eq. 2.12 becomes,

$$f(x,y)=\int_0^{\pi}\left[\int_{-\varepsilon}^{\varepsilon}P(\eta,\tau)|\tau|L(\tau)e^{2\pi i\tau x'}d\tau\right]d\eta \tag{2.14}$$

where $L(\tau)$ is a low pass filter. An example of a low pass filter is the Hamming filter ($H(\tau)$) which is given by [18, 22],

$$H(\tau)=\begin{cases}0.1\cos\left(\frac{2\pi\tau}{\tau_{cut}}\right) & \text{if} \quad |\tau|\le\tau_{cut}\\ 0 & \text{if} \quad |\tau|>\tau_{cut}\end{cases} \tag{2.15}$$

where τ_{cut} is the cut of frequency of the Hamming filter. The value of τ_{cut} determines the noise and resolution of the reconstructed image [22]. If τ_{cut} is set to a lower frequency than ε, the noise in the reconstructed image will be reduced at the expense of spatial resolution [22].

Using the convolution theorem, Eq. 2.14 can be rewritten as [20],

$$f(x,y)=\int_0^{\pi}P(\eta,x')*G(x')=\int_0^{\pi}\left[\int_{-\infty}^{\infty}P(\eta,x')G(x\cos(\eta)+y\sin(\eta)-x'')dx''\right]d\eta, \tag{2.16}$$

where $G(x')$ is the 1D inverse Fourier transform of $|\tau|\cdot L(\tau)$.

The FBP algorithm presented in Eq. 2.16 can only be used to reconstruct cross-sectional images of an object if 1D X-ray projections are acquired in parallel beam geometry as illustrated in figure 2.5a. For reconstruction of cross-sectional images of an object from 1D X-ray projections acquired in equispaced fan-beam geometry as illustrated in figure 2.5b, the FBP algorithm for parallel beam 1D X-ray projections in Eq. 2.16 must be adapted to the fan-beam geometry. A simple illustration of the fan beam image reconstruction problem is presented in figure 2.7. In this figure, the X-ray source is assumed to rotate in a circle with radius $R(-\sin(\beta),\cos(\beta))$ around a virtual detector placed at

the origin of the Cartesian coordinate system [17]. The cross-sectional image of the object is to be reconstructed and described in the Cartesian coordinate system as function of x and y.

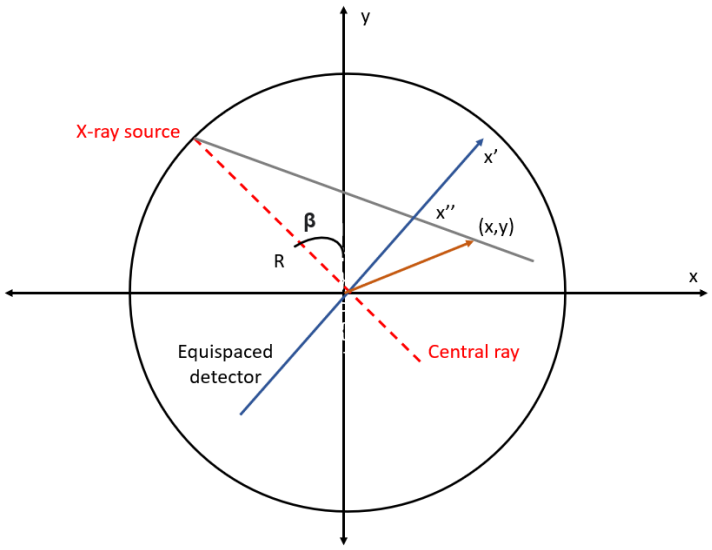

Figure 2.7: *Illustration for equispaced fan beam image reconstruction problem. Adapted from Shaw [17].*

The FBP for 1D X-ray projections acquired equispaced fan-beam geometry can be expressed as [17, 21]:

$$f(x,y) = \frac{1}{2}\int_0^{2\pi} \frac{R^2}{(R + x\sin(\beta) - y\cos(\beta))^2} \int_{-\infty}^{\infty} P(\beta, x') \frac{R}{\sqrt{R + x'^2}} \cdot G(x'' - x')\, dx'\, d\beta, \tag{2.17}$$

with

$$x'' = R\frac{y\sin(\beta) + x\cos(\beta)}{R + x\sin(\beta) - y\cos(\beta)}, \tag{2.18}$$

where:

- $R + x\sin(\beta) - y\cos(\beta)$: is the distance between the X-ray source and the projection of pixel with coordinate (x, y) onto the central ray.
- β: is the angle between the central ray and the y-axis.
- $P(\beta, x')$: is a fan beam X-ray projection.
- x'': is a position on the virtual equispaced detector.

X-ray cone-beam CT can also be divided in two steps: 1) acquisition of cone-beam X-ray projections, and 2) 3D image reconstruction. During the acquisition of the cone-beam X-ray projections, an X-ray source emitting a cone-shaped beam of X-ray photons and a 2D X-ray detector rotate around the object. The intensity of the transmitted X-ray photons is measured by a 2D X-ray detector and used to form cone-beam X-ray projections of the object. Three-dimensional (3D) images of the object can then be reconstructed using the values of the cone-beam X-ray projections as input in a 3D image reconstruction algorithm [19]. The most commonly used 3D image reconstruction algorithm for cone-beam X-ray projections acquired along a circle is the Feldkamp, Davis and Kress (FDK) algorithm [23]. The Feldkamp, Davis and Kress algorithm is the extension of the FBP algorithm for equispaced fan-beam geometry presented in Eq. 2.17. The geometry for the cone-beam image reconstruction problem is illustrated in figure 2.8.In this geometry the X-ray source is assumed to rotate in a circle with a radius R(which is not shown in the figure 2.8). A

virtual 2D flat X-ray detector(this can be the representation of indirect X-ray detector in the CBCT imaging system of the XenX that was presented in section 2.2) is positioned at the origin along the z-axis.

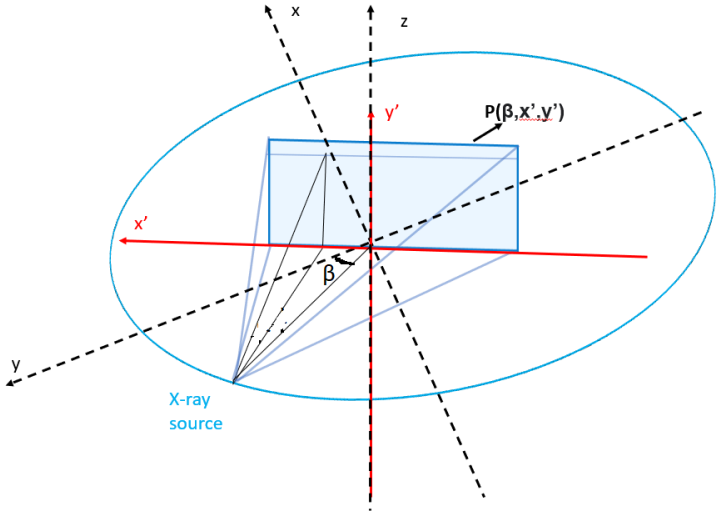

Figure 2.8: *Geometry for the cone-beam image reconstruction problem. Adapted from Shaw [17]*

The Feldkamp, Davis and Kress algorithm for a 2D flat X-ray detector may be expressed as the following [17]:

$$f(x,y) = \frac{1}{2}\int_0^{2\pi} \frac{R^2}{(R + x\sin(\beta) - y\cos(\beta))^2} \int_{-\infty}^{\infty} P(\beta, x', y'') \frac{R}{\sqrt{R + x'^2 + y''^2}} \cdot h(x'' - x')\, dx'\, d\beta, \tag{2.19}$$

where:

- (x', y''): are coordinate for the 2D flat X-ray detector. x' in Eq. 2.19 is the same as Eq. 2.18 and y'' Eq. 2.19 is given by:

$$y'' = \frac{z \cdot R}{R + x\sin(\beta) - y\cos(\beta)} \tag{2.20}$$

- $P(\beta, x', y'')$: is a cone-beam X-ray projection.

The FDK reconstruction algorithm performs an exact reconstruction of $f(x,y)$ in the plane defined by the circle of R along which the X-ray source and 2D flat X-ray detector rotate around the object [17]. The further away from this plane along the z-axis the less accurate the FDK reconstruction algorithm is to estimate $f(x,y)$ [17].

After image reconstruction, the attenuation coefficient in each voxel of the CBCT image is converted to Hounds-field Units HU by using the following expression [16],

$$HU = 1000\left(\frac{\mu - \mu_{water}}{\mu_{water} - \mu_{air}}\right), \tag{2.21}$$

where:

- μ: is the attenuation coefficient of the material in the object corresponding to the voxel's position in the CBCT image.
- μ_{water}: is the attenuation coefficient of water.

  μ_{air}: is the attenuation coefficient of air.

From the definition of the HU in equation (2.21) it follows that the HU for air is -1000 and the HU for water is 0 [24].

2.5 Noise and ring artefacts

Noise degrades the quality of CBCT images. Noise is statistic fluctuations in the detected signal. Because the cone beam X-ray projections are formed based on this signal, the cone-beam X-ray projections also contain noise. The noise in the cone-beam X-ray projections is subsequently transferred to the CBCT image of an object during reconstruction when using the FDK algorithm. There are two major contributions to the overall noise observed in CBCT images, electronic noise, and quantum noise [25]. The electronic noise comes from the electrical components used to read out the signal from the X-ray detector [25]. Quantum noise is associated with the uncertainty in the number of detected X-ray photons [25].

Ring artefacts are ring-shaped structures that appear in the reconstructed image. Figure 2.9 shows an axial CBCT image of a mouse phantom which contains several ring artefacts .

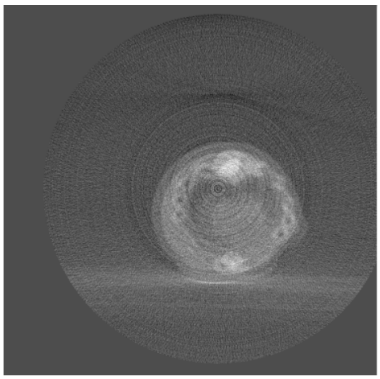

Figure 2.9: *Axial CBCT image of a mouse phantom which contains several ringartefacts.*

These ring artefacts may be caused by bad calibration of the X-ray detector and by defective element of the X-ray detector [18].

2.6 Image segementation

Image segmentation is a process employed to divide an image into different regions [15, 17]. In a CBCT image, different materials have different HU. One method of image segmentation is thresholding. Thresholding works in the following manner [17]:

1. A histogram of HU values in the image is generated.
2. From the histogram of the image a minimum or maximum HU value is set.
3. All voxels with HU values greater than or lower than the defined maximum or minimum HU belong to the object of interest.

Contrast, noise, and spatial resolution are three factors that affect the performance of the thresholding segmentation method. In an image with good contrast, it is easy to identify objects. On other hand, if an image has poor contrast, it will be difficult to differentiate objects from each other in the image. Noise affects the image by causing fluctuation in HU between voxels and therefore makes it difficult to differentiate different objects or structures in the image. Noise further complicates image segmentation by making the choice of an appropriate threshold more ambiguous during thresholding [20]. The spatial resolution also affects the edges in an image. Therefore, if an image has a poor spatial resolution, it will be difficult to segment it because it is uncertain what objects are being separated in the image. To facilitate image segmentation it is, therefore, necessary for the image to have good contrast, contain as low a level of noise as possible, and have good spatial resolution. Furthermore, all types of image artefacts should be removed completely or reduced from an image before image segmentation.

2.7 Treatment planning

Figure 2.10 depicts a flowchart which describes the typical steps in the treatment planning process for SAEBRT [26].

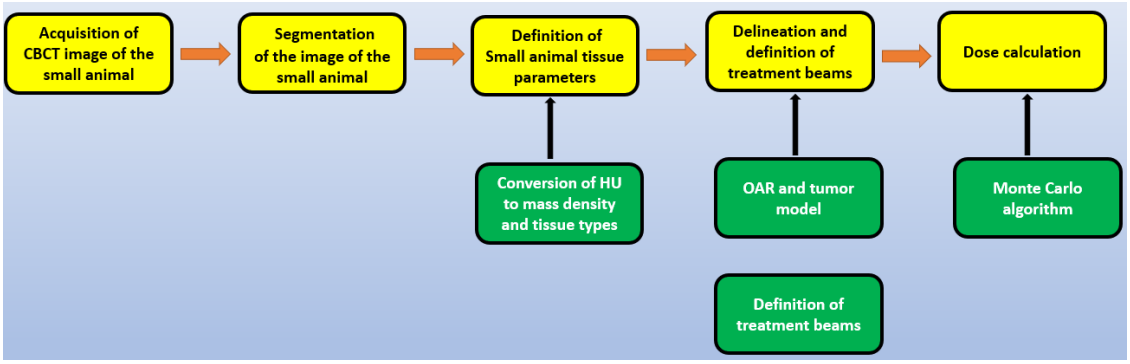

Figure 2.10: *Common steps in the treatment planning process for SAEBRT.*

The treatment planning process starts with the acquisition of the CBCT image of the part of the small animal which will receive the treatment, and by importing the acquired CBCT image to a TPS for SAEBRT.

In the TPS, the acquired CBCT image is segmented. The segmentation of the CBCT image can be performed by using the thresholding segmentation method presented in section 2.8.

After segmentation of the CBCT image, the tissue parameters (mass density and elemental composition of tissues) of the small animal are defined in the following manner:

1. The HU value in each voxel of the CBCT image of the small animal is converted into mass density.
2. The mass density is used to assign a material (with specific elemental composition) to each voxel of the CBCT image.

The assignment of tissues to the voxels of the CBCT images of small animals is challenging because the elemental composition of tissues in small animals is unknown [9]. The common strategy employed to assign tissues with a specific elemental composition is to assume that small animals all consist of the same type of tissues present in the human body and then assign human tissues to each voxel of the CBCT of the small animals [9].

Following the definition of the tissue parameters of the small animal, the target volume and organs at risk (OAR) in the acquired CBCT image of the small animal are delineated [26].

After delineation of the tumour and OAR, a set of treatment beams are defined by determining their orientation, shape, size, and energy [26]. Small animal external beam radiotherapy uses small kV photon beams with a diameter typically less than 10 mm (for cylindrical treatment beams) to accurately deliver the dose to the tumour in the small animals [26].

After the definition of the treatment beams, the dose distribution in the delineated tumour and OAR in the CBCT image of the small animal is estimated using a dose calculation algorithm in the TPS for SAEBRT. For the treatment of small animals with kV photon beams, the MC dose calculation algorithm provides the most reliable estimation of the distribution of the dose within the medium of the small animals [9]. The MC dose calculation algorithm simulates the interaction of particles and secondary particles in the medium of interest [27, 28]. Each particle is associated with a history which describes the events that it undergoes. The MC dose calculation algorithm uses probability distributions of the interactions and pseudorandom numbers to simulate the relevant interactions [28, 29]. The simulated particles are obtained from the phase space of the actual beam [28]. Using a pseudorandom number, the MC dose calculation algorithm computes the mean free path for each particle from the phase file and the particles are transported the distance corresponding to the computed mean free path to the position of the next interaction in the medium of interest [28, 29]. At the position of interaction, the MC dose calculation algorithm uses another pseudorandom number to determine the next interaction that will occur [28]. Once the interaction has been determined,

the interaction is simulated by the MC dose calculation algorithm, and if secondary particles are produced, they are also simulated [28]. This procedure is repeated until the energy of the secondary particle is below the certain threshold energy [28, 29]. The energy of the secondary particles is considered to be absorbed locally in the medium of interest when it is below the threshold energy [28, 29].

2.8 Dosimetry with radiochromic film

In external beam radiotherapy, radiochromic films are used for radiation dosimetry. These radiochromic films have the following properties [1, 30]:

- They have a high spatial resolution.
- They are self-developing, that is they do not require any processing before the readout.

A typical radiochromic film consists of an active layer of di-acetylene of monomer and two layers of polyester which are arranged as shown in figure 2.11 [1].

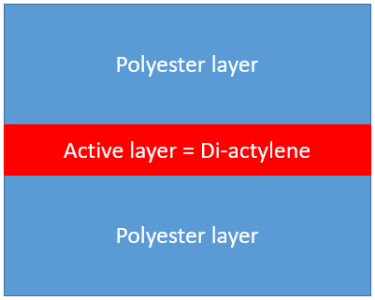

Figure 2.11: *Arrangement of the different layers in a typical radiochromic film.*

The radiochromic film works as follows [1]:

1. The ionising radiation enters the active layer and interacts with the material of the active layer.
2. Interaction between the material of the active layer and the ionising radiation causes polymerisation which results in the dark colouring of the radiochromic film.
3. The optical density of the radiochromic film is proportional to the dose of radiation delivered to it.
4. The polymerisation process continues until 24 hours after the irradiation of the radiochromic films and then stabilises.

Figure 2.12 illustrates the working principle of radiochromic films by showing two radiochromic films, one which has been exposed to a beam of X-ray photons generated by the XenX, and one unexposed.

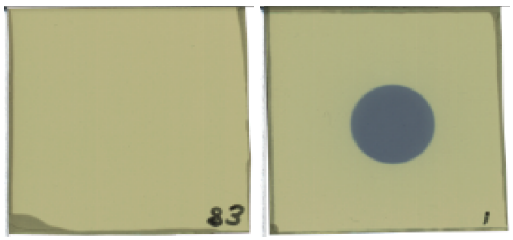

(a) (b)

Figure 2.12: *Colour change of radiochromic film caused by exposure to X-ray photons generated by the XenX. Unexposed radiochromic film (a) and exposed radiochromic film (b).*

Chapter 3

Materials and methods

3.1 Phantoms

In the first part of this thesis, a cylindrical water phantom, a metallic grid of holes, and a 3D printed mouse phantom (Leeds Test objects, Boroughbridge, UK) were used. Figure 3.1 shows a photograph of the cylindrical water phantom, metallic grid of holes, and 3D printed mouse phantom.

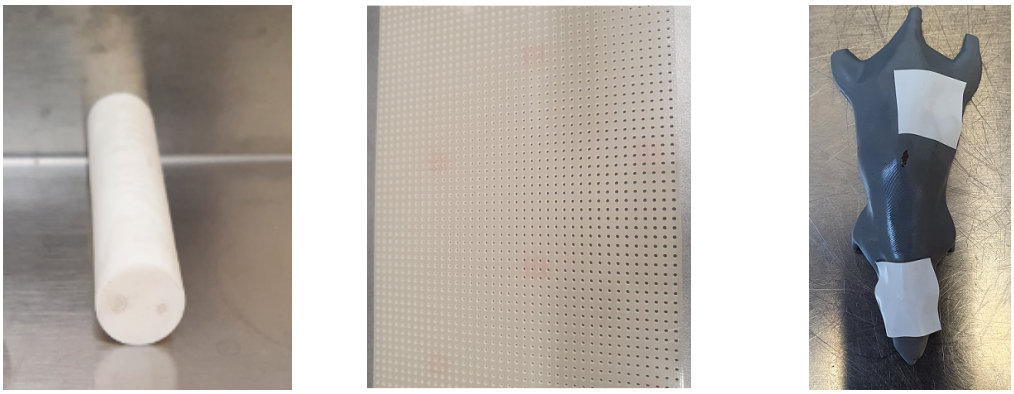

(a) (b) (c)

Figure 3.1: *Photograph of the cylindrical water phantom (a), metallic grid of holes (b) and 3D printed mouse phantom (c).*

The cylindrical water phantom (diameter = 9cm and height = 2cm) was constructed at the institution and was filled with water. The distance between the holes in the metallic grid was 4 mm and each hole had a diameter of 1 mm. The 3D printed mouse phantom consisted of three different types of materials which were all made of special polymers, one polymer to simulate bone (density $\rho = 1.78$ g/cm^3), and the remaining two polymers to simulate lung ($\rho = 0.24$ g/cm^3) and soft tissue ($\rho = 1.03$ g/cm^3).

In the second part of this thesis, four slab phantoms were used. The four slab phantoms (Phantom 1, Phantom 2, Phantom 3, and Phantom 4) were constructed with different slabs that consisted of polystyrene (PS) ($\rho = 1.1$ g/cm^3), aluminium (AL) ($\rho = 2.7$ g/cm^3), and cork (CO) ($\rho = 0.3$ g/cm^3). The thickness of each slab was 2 mm and the area of each slab was 35×35 mm^2. The four slab phantoms are described in table 3.1 and figure 3.2 shows a photograph of the four slab phantoms.

Table 3.1: *Description of the four slab phantoms.*

Phantom	**Construction**	**Total thickness** [mm]
1	2 mm (PS) × 7	14
2	2 mm (PS) × 2 + 2 mm (AL) × 2 + 2 mm (PS) × 3	14
3	2 mm (PS) × 2 + 2 mm (CO) × 3 + 2 mm (PS) × 2	14
4	2 mm (PS) × 2 + 2 mm (AL) + 2 mm (CO) × 3 + 2 mm (AL) + 2 mm (PS) × 2	18

(a) (b) (c) (d)

Figure 3.2: *Photograph of Phantom 1 (a), Phantom 2 (b), Phantom 3 (c), and Phantom 4 (d).*

3.2 Acquisition of cone-beam X-ray projections

The cylindrical water phantom and 3D printed mouse phantom were positioned separately at the isocenter on the stage in the XenX using its lasers for guidance. Cone-beam X-ray projections of the 3D printed mouse phantom and cylindrical water phantom were successively acquired using the XenX's CBCT imaging system. In addition, flat field X-ray projections were also acquired. The acquisition parameters were the same for all acquisitions and are presented in table 3.2.

Table 3.2: *Acquisition parameters.*

Parameter	**Value**	**Unit**
Voltage	60	kV
Current	0.8	mA
Number of cone-beam X-ray projections	360	
Angular range	[0,359]	°
Angular increment	1	°
Acquisition time	67	s

3.3 MuriSlice

MuriSlice is the software that is used in this thesis to reconstruct CBCT images from the cone-beam X-ray projections of the objects. The software consists of three parts: a pre-possessing part, an image reconstruction part, and a post-processing part [31]. The parameters in the post-processing part were not investigated in this thesis.

The pre-processing part consists of three different filters (denoted pre-filters) which are used to reduce the noise in the cone-beam X-ray projections [31]. The three pre-filters are: a Gaussian low-pass pre-filter, a median pre-filter, and an edge-preserving pre-filter [31]. The operator can select median pre-filters and Gauss low-pass pre-filters with

3×3 and 5×5 kernel sizes [31]. The Gaussian pre-filter and median pre-filter reduce the noise in cone-beam X-ray projections at expense of spatial resolution. To reduce noise with less degradation of the spatial resolution, the edge-preserving denoising pre-filter uses an iterative procedure for noise reduction. This procedure is controlled by the number of iterations [31]. The operator can select the number of iterations [31], which can vary from two to ten in steps of one [31]. In the pre-processing part, the operator can also select the size of the voxel that will be used to reconstruct the image.

In the reconstruction part, the images are reconstructed from the filtered cone-beam X-ray projections using the FDK algorithm described in Eq. 2.19 with the Hamming filter [31].

In this thesis, all images reconstructions were performed on a desktop computer (model:Precision T7910, Dell, Texas, USA) with Intel Xenon CPU E5–2637 with 32 GB RAM. The reconstructed images were stored in the DICOM (digitally image and communications in medicine) file format. After image reconstruction, the computed attenuation coefficients in the voxels of reconstructed images were directly converted into voxel values by MuriSlice. For treatment planning, the voxel values were converted to Hounsfield units by the MuriSlice software based on a calibration which was done with a water phantom [32].

3.4 Optimisation criteria

The criteria for optimisation of the CBCT reconstruction protocol in MuriSlice were the following:

1. to reduce as many ring artefacts and as much noise as possible from the reconstructed CBCT images.
2. to obtain as high spatial resolution as possible in the reconstructed CBCT images.
3. to obtain as high contrast resolution as possible between the different structures in the reconstructed CBCT images.

3.5 CBCT image reconstructions with different voxel sizes

The cone-beam X-ray projections of the cylindrical water phantom were loaded into MuriSlice. Three CBCT images were reconstructed with three voxel sizes: $(100\ \mu m)^3$, $(200\ \mu m)^3$ and $(300\ \mu m)^3$.

3.6 External corrections

The cone-beam X-ray projections of the 3D printed mouse phantom and flat field X-ray projections were processed separately in different ways referred to as external corrections to prepare them for CBCT image reconstruction. These external corrections were performed in different computer programs. A flowchart which describes the external corrections and how they were applied on the cone-beam X-ray projections of the 3D printed mouse phantom and flat field X-ray projections in the different computer programs is presented in figure 3.3.

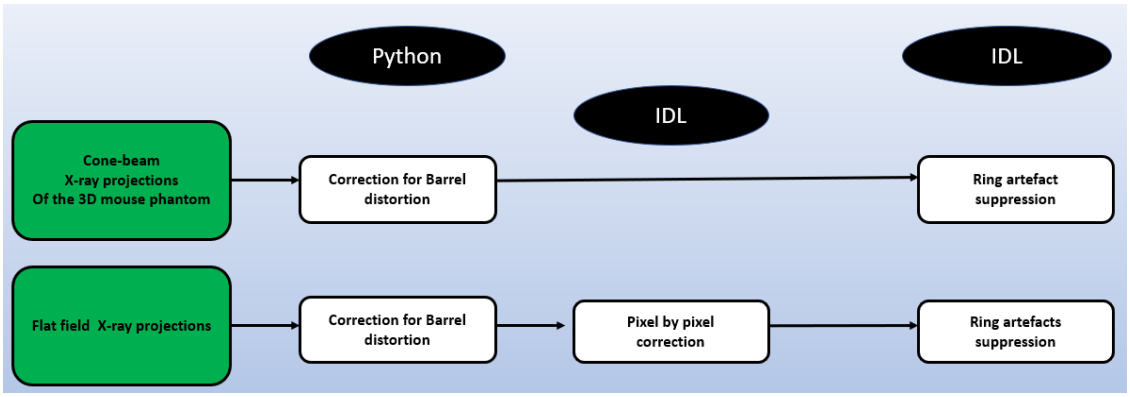

Figure 3.3: *Flowchart describing how the external corrections (shown in the white boxes) were applied to the cone-beam X-ray projections of the 3D printed mouse phantom and flat field X-ray projections (shown in the green boxes) in the different computer programs (shown in the black circles).*

The external corrections included: a correction for the Barrel distortion, pixel-by-pixel correction, and ring artefacts suppression. The correction for the Barrel distortion was done in the Python programming language (Version 3.7) [33]. The pixel-by-pixel correction and the ring artefacts suppression were both performed in the IDL programming language (Version 8.8, Exelis Visual Information Solutions, Boulder, Colorado, USA).

3.6.1 Correction for Barrel distortion

The cone-beam X-ray projections of the 3D printed mouse phantom and flat field X-ray projections suffered from a distortion called Barrel distortion [34, 35]. Figure 3.4 shows a cone-beam X-ray projection of the 3D printed mouse phantom which contains the Barrel distortion.

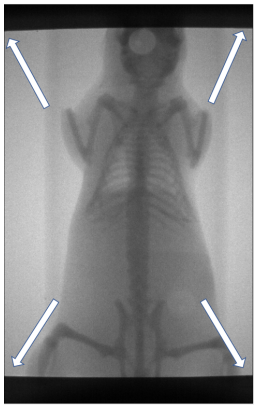

Figure 3.4: *Barrel distortion in a cone-beam X-ray projection of the 3D printed mouse phantom. The Barrel distortion is noticeable at the periphery of the cone-beam X-ray projection as indicated by the white arrows.*

To correct the Barrel distortion, the python script developed by Nghia [1] was used. This Python script is based on the method for correction of Barrel distortion proposed by Nghia *et al.* [35]. More details on this method can also be found in [36] and [34]. The method consists of two parts, a calibration part and a correction part which are explained in detail in Appendix C.

[1] The Python script is copyrighted and available for free at: https://github.com/nghia-vo/vounwarp

3.6.2 Pixel-by-pixel correction

The pixel values in the Barrel undistorted flat field X-ray projections which were acquired at different projection angles varied. To reduce the variation, a pixel-by-pixel correction was applied to them. The pixel-by-pixel correction was performed by computing a mean Barrel undistorted flat field X-ray projection with pixel values ($\overline{P(x,y)}$) given by,

$$\overline{P(x,y)} = \frac{1}{\vartheta}\sum_{i=0}^{\vartheta} P(x,y)_i, \text{ for } x \in \{1, ..., N_x\} \text{ and } y \in \{1, ..., N_y\}. \tag{3.1}$$

Where:

- $P(x,y)_i$: denote the pixel values in a Barrel undistorted flat field X-ray projections.
- N_x = 1200: denotes the number of columns of the Barrel undistorted flat field X-ray projections.
- N_y = 1920 pixels: denotes the number rows of a Barrel undistorted flat field X-ray projections.
- ϑ = 359: denotes the total number of Barrel undistorted flat field X-ray projections.

3.6.3 Ring artefacts suppression

To reduce the rings artefact in the reconstructed CBCT images of the 3D printed mouse phantom, the following special 2D Butterworth filter was used to filter the sinograms of the Barrel undistorted cone-beam X-ray projections of 3D printed mouse phantom and the mean Barrel undistorted flat field X-ray projection [37],

$$B(u,v) = \begin{cases} \dfrac{1}{1+(\frac{u}{u_0})^{2n}} & |v| \leq v_0 \\ 1 & \text{otherwise} \end{cases}. \tag{3.2}$$

Where:

- u and v: denotes horizontal and vertical spatial frequencies.
- n: denotes the order of the 2D Butterworth filter.
- u_0: denotes the horizontal cut-off frequency of the 2D Butterworth filter.
- v_0: denotes vertical cut-off frequency of 2D Butterworth filter

A Nyqvist frequency of 85 cm^{-1} was calculated by using the following expression,

$$F_N = \frac{1}{2\Delta x} \tag{3.3}$$

where Δx denotes the side of a pixel and was obtained from the specification of the digital camera in table B.1. The horizontal cut-off frequency was set to 5 cm^{-1} as recommended by Catsen *et.al.* [37]. Catsen *et.al.* recommended to use a cut-off frequency much lower than the Nyquist frequency [37]. The order was set to 4 as recommended by Casten *et.al.* [37].

3.7 CBCT image reconstructions with and without external corrections

Once all external corrections were completed, the corrected cone-beam X-ray projections, and the mean flat field X-ray projection were loaded into MuriSlice. To visually inspect the effect of all external corrections, two CBCT images of the 3D printed mouse phantom were reconstructed. One image was reconstructed using uncorrected cone-beam X-ray projections and flat field X-ray projections. The other image was reconstructed using the corrected cone-beam X-ray projections and mean flat field X-ray projection. The two images were reconstructed with a voxel size of $(100\ \mu m)^3$.

3.8 CBCT image reconstructions with different pre-filters

Following all external corrections, the corrected cone-beam X-ray projections, and the mean flat field X-ray projection were loaded into MuriSlice, where six different pre-filters were tested for noise reduction. The six different pre-filters were: the median pre-filter with 5×5 kernel (M5×5), median pre-filter with 3×3 kernel (M3×3), Gaussian low-pass pre-filter with 5×5 kernel (G5×5), Gaussian pre-filter with 3×3 kernel (G3×3), the edge-preserving denoising pre-filter with 2 iterations (EPIT2), and the edge-preserving denoising pre-filter with 10 iterations (EPIT10). For each pre-filter, a corresponding CBCT image of the 3D printed mouse phantom was reconstructed with a voxel size of $(100\ \mu m)^3$.

3.9 Evaluation of image quality

Image J (National Institutes of Health, Maryland, USA) was used to define a square regions of interest (ROI) with an area of 132 mm^2 at the centre of the same axial image from each of the three images of the cylindrical water phantom obtained in section 3.5. The signal-to-noise ratio (SNR) in the ROI was calculated with the following expression,

$$SNR = \frac{S_{VS}}{\sigma_{VS}},\ \text{for VS} \in \{(100\mu m)^3, (200\mu m)^3, (300\mu m)^3\} \tag{3.4}$$

where:

- VS: denotes a voxel size.
- S_{VS}: denotes the mean of voxel values in the ROI in the axial image of the cylindrical water phantom that was reconstructed with VS.
- σ_{VS}: is the standard deviation of voxel values in the ROI in the axial image of the cylindrical water phantom that was reconstructed with VS.

A graphical user interface developed in IDL (version 8.5) was used to define two ROI in the same axial images from the six CBCT images of 3D printed mouse phantom obtained in section 3.8 to obtain the mean of the voxel values and the standard deviations in the voxel values in these two ROI. One of the ROI contained 11 voxels and was defined in the structure representing soft tissue in the axial images. The other ROI contained 12 voxels and was defined in the structure that represented bone in the axial images. The signal-to-noise ratio (SNR_{st}) in the ROI in the structure that represented soft tissue in each axial image of the was calculated using,

$$SNR_{st} = \frac{S_f}{\sigma_f},\ f \in \{M5\times5, M3\times3, G5\times5, M3\times3, EPIT2, EPIT10\} \tag{3.5}$$

where:

- f: denotes a pre-filter.
- S_f: denotes the mean of voxel values in the ROI in the structure that represented soft tissue in the axial image of the 3D printed mouse phantom that was reconstructed by using cone-beam X-ray projections of the 3D printed mouse phantom which were filtered with f.
- σ_f the denotes the standard of voxel values in the ROI in the structure that represented soft tissue in the axial image of the 3D printed mouse phantom that was reconstructed by using the cone-beam X-ray projections of the 3D printed mouse phantom which were filtered with f.

The contrast-to-noise ratio (CNR_{bs}) between the structure that represented soft tissue and bone in each axial CBCT images was calculated as,

$$CNR_{bs} = \frac{(S_{b,f} - S_{s,f})}{\sigma_{s,f}}, \tag{3.6}$$

where:

- s: denotes the structure that represented soft tissue in a the axial image of the 3D printed mouse phantom.
- b: denotes the structure that represented bone in the same axial image of 3D printed mouse phantom.
- $S_{b,f}$: denotes the mean of voxel values in the ROI in bone.
- $S_{s,f}$: denotes the mean of voxel values in an ROI in soft tissue.
- $\sigma_{s,f}$ the standard deviation of the voxel values in the ROI in soft tissue.

3.10 μRayStation 8B

μRaystation 8B is the treatment planning system for SAEBRT that is used in this thesis. μRaystation 8B uses CBCT images to model the anatomy of small animals and for calculation of the dose that is administrated to the small animals during SAEBRT [38]. μRaystation 8B uses a Monte Carlo algorithm called Voxel based Monte Carlo (VMC++) for dose calculation [38]. This Monte Carlo algorithm uses a technique called Class II condensed history (CH) to simulate the transport of electrons [38]. The Monte Carlo algorithm also uses the phase space file for the actual treatment beam of the XenX to simulate the interaction of X-ray photons that results in secondary X-ray photons with energy above a certain energy threshold denoted E_γ and the inelastic scattering of electrons that results in the creation of electrons with energy above certain threshold energy denoted E_δ [38]. The inelastic scattering of electrons with lower energy than E_δ is treated using Continuous Slowing Down Approximation (CSDA), that is the electrons are assumed to lose their energy continuously in the medium when their energy is lower than E_δ. For dose calculation E_γ and E_δ are set to 10 keV.

To perform dose calculation with the Monte Carlo algorithm, the voxels of the CBCT image must be assigned tissues with specific elemental composition [39]. At low X-ray photon energy, the Compton scattering, and photoelectric absorption dominate, therefore the cross-sections for these two X-ray interactions are needed for simulations of these two X-ray interactions in the medium. To simulate interactions of electrons in the medium, the collision stopping power, radiation stopping power, and scattering power are needed. To determine the cross-section for Compton scattering, the cross-section for photoelectric absorption, collision stopping power, radiation stopping power, and scattering power, the atomic number of the tissues in the voxels of the CBCT image must be known [40]. To determine the tissues in the voxels of the CBCT image μRaystation 8B uses two different approaches. The first approach involves the following steps:

1. The use of a CBCT Hounsfield unit to mass density calibration to convert the HU in the voxels of the CBCT image into mass density.
2. The mass densities are then used to assign tissues to the voxels. The tissues that are assigned to the voxels of the CBCT image are obtained from an internal list in μRaystation 8B that consist of 50 human tissues. These 50 human tissues have been obtained through linear interpolation in a list of 10 materials of known elemental composition consisting of air, lung, adipose, tissue, muscle, cartilage, bone, aluminium, iron, gold, and osmium [38, 39].

The second approach involves the following steps:

1. Manual delineation of the region of interest in the CBCT image of the small animal.
2. The voxels in the region of interest are then assigned a fixed mass density.
3. The mass densities were assigned to the voxels in region of interest with the first approach are replaced the fixed mass densities [38].
4. The fixed mass densities are then used to assigned tissues to voxels in the region of interest.

3.11 Radiochromic film measurements and treatment planning

Gafchromic EBT3 (Ashland Speciality ingredients G.P., Bridgewater, New Jersey, USA) films were placed at different depths in the four slab phantoms. The different depths are shown in table 3.3. Hereafter, Gafchromic EBT3 films will be referred to as EBT3 films. The EBT3 film batch was calibrated in a clinical 200 kV beam against an ionisation chamber before this thesis. The calibration factors were traceable to a standard laboratory. The area of each ETB3 film was 33×33 mm^2 and each ETB3 film consisted of a 28 μm thick active layer which was enclosed by two 125 μm layers of matte-polyester.

Table 3.3: *Depth at which the ETB3 films were positioned in each slab phantom.*

Phantom name	**Depth [mm]**
Phantom 1, 2 and 3	0, 2, 4, 6, 8, 10, 12 , 14
Phantom 4	0, 2, 4, 6, 8, 10, 12 , 14, 16, 18

Each slab phantom was separately positioned at the isocenter in the XenX using its laser for guidance and treated with a circular treatment beam generated by the XenX's treatment system. Each slab phantom was treated three times and treatment parameters are given in table 3.4. Additionally, 6 films were not treated but used as unexposed backgrounds for film analysis.

Table 3.4: *Treatment parameters*

Parameter	**Value**	**Unit**
Gantry angle	0	°
Tube current	13	mA
Tube voltage	220	kV
Treatment time	180	s
Treatment dose	10	Gy
Diameter of treatment beam	10	mm
Source to surface distance	34.5	mm

The following expression obtained from the calibration of the EBT3 films was used to determine the dose D that was delivered to each ETB3 film,

$$D = 3.1 \cdot \left(\frac{I_0}{I}\right)^2 - 3.1 \cdot \left(\frac{I_0}{I}\right) - 0.3 \text{ [Gy]}, \tag{3.7}$$

where:

- I_0: denotes the mean of the grayscale values in a ROI in the scanned image of unexposed EBT3 film.
- I: denotes is the mean of the grayscale values in a ROI in the scanned image of the exposed EBT3 film.

As mentioned in section 2.8 the polymerisation of EBT3 films continues after the irradiation of the radiochromic film and then stabilises. Therefore, the EBT3 films were scanned using a flatbed scanner (Epson Expression 12000XL, Seiko Epson Corporation, Nagano, Japan) and analysed in Image J 24 hours after treatment. During the calibration of the ETB3 films, the ETB3 films were also scanned 24 hours after irradiation. The mean of grayscale values in ROI in the scanned image of exposed and unexposed EBT3 films obtained during the analysis of the EBT3 films was inserted in (3.7) to obtain the dose delivered to each EBT3 film. After the calculation of D, the average dose delivered to the EBT3 films was calculated. The calculated average dose delivered to the EBT3 films was then converted to the dose D_M to each the material M in the slab phantoms by using the following expression,

$$D_M = D_{polyester} \cdot \frac{\sum_{i=0}^{N} \Phi_i \cdot E_i \cdot \left(\frac{\mu_{en}}{\rho}\right)_{M,E_i}}{\sum_{i=0}^{N} \Phi_i \cdot E_i \cdot \left(\frac{\mu_{en}}{\rho}\right)_{polyester,E_i}} \text{ for } M \in \{PS, AL, CO\} \tag{3.8}$$

where:

- $D_{polyester}$: denotes the dose delivered to the polyester layer of an EBT3 film and was assumed to be the same as the average dose delivered active layer of the EBT3 film.
- E_0=E_{min}: denotes the lowest X-ray photon energy in the calculated analytical X-ray photon fluence spectra for the XenX's 220 kV beam of X-ray photon which was used as input in μRayStation 8B.
- E_N=E_{max}: denotes the highest X-ray photon energy in the calculated analytical X-ray photon fluence spectra for the XenX's 220 kV beam of X-ray photon that which was used as input in μRayStation 8B.
- Φ_i: is the normalised fluence of X-ray photon with energy E_i and was obtained from the normalised X-ray photon fluence spectra for the XenX's 220 kV beam of X-ray photon in Appendix D.
- $\left(\frac{\mu_{en}}{\rho}\right)_{M,E_i}$: the mass energy absorption coefficient for the X-ray photon with energy E_i in the material of the slab phantoms.
- $\left(\frac{\mu_{en}}{\rho}\right)_{polyester,E_i}$: denotes the mass energy absorption coefficient for the photon with energy E_i in the polyester.

The mass energy absorption coefficients for aluminium and polystyrene were obtained from the National Institute of Standards and Technology (NIST) [41]. No mass energy absorption coefficient for cork was available in NIST. Therefore, the mass energy absorption coefficient for cork was calculated using the mass energy absorption coefficient for lung taken from NIST [41]. To compensate for the difference in electron density in lung and cork, the energy mass absorption for lung was multiplied by the electron density ratio of natural cork and lung to obtain the energy mass absorption for cork. The electron density for lung and natural cork was obtained from Fuse et al. [42].

Following the treatment, cone-beam X-ray projections of each slab phantom were acquired using the XenX's CBCT imaging system with the same acquisition parameters as in table 3.2. The Barrel distortion correction and the ring artefacts suppression were applied to the cone-beam X-ray projections. The corrected cone-beam X-ray projections were loaded into the MuriSlice. In MuriSlice, CBCT images of the slab phantoms were reconstructed using the following reconstruction parameters: the EPIT10 pre-filter, FDK algorithm, Hamming filter, and a voxel size of $(100\,\mu m)^3$. Once image reconstruction had been performed, the images were exported to μRayStation 8B for treatment planning. The treatment planning started by segmentation of the images into different regions using the tool for image segmentation available in μRayStation 8B. The segmentation tool segments the images with the thresholding segmentation method. After image segmentation, the voxels of the CBCT image of the slab phantoms were assigned mass densities and materials based on the CBCT Hounsfield unit to mass density calibration or by manual identification. The CBCT Hounsfield unit to mass densities calibration was created in μRayStation 8B with the materials that are given in table 3.5.

Table 3.5: *Mass density and Hounsfield unit for material used to create the Hounsfield unit to mass density calibration in μRayStation 8B.*

Material	Hounsfield unit [HU]	Mass density [g/cm^3]
Air	-1000	0.0012
Water	0	1.03
Bone	900	1.78
Aluminium	2972	2.7

The Hounsfield unit and density for aluminium and air were already defined in μRayStation 8B. The mass density for water and bone and the Hounfield unit for bone were provided by Xstrahl. After assigning density to the voxels of the CBCT image of slab phantoms, materials were assigned based on CBCT Hounsfield unit to mass densities calibration or by manual identification. Following material assignment, dose calculation was performed on the CBCT images of the slab phantom with the VMC++ dose calculation algorithm in μRayStation. The number of histories was set to 1 million and the calculation grid had a resolution of $(200\,\mu m)^3$. Finally, the calculated percentage depth dose (PDD) curves along the central axis of the beam was exported from μRayStation for comparison with the EBT3 film measurements.

Chapter 4

Results

4.1 Evaluation of image quality

The calculated signal to noise ratios in the defined ROI in the axial images of the cylindrical water phantom are presented in table 4.1 along with the corresponding the voxel sizes. From table 4.1 it is observed that the SNR increases between $(100\,\mu\text{m})^3$ and $(200\,\mu\text{m})^3$ and then decreases between $(200\,\mu\text{m})^3$ and $(300\,\mu\text{m})^3$.

Table 4.1: *The calculated SNR with corresponding voxel sizes.*

VS	SNR
$(100\,\mu\text{m})^3$	339
$(200\,\mu\text{m})^3$	1186
$(300\,\mu\text{m})^3$	583

Figure 4.1 shows a diagram of the calculated signal to noise ratios in defined ROI in the structure that represented soft tissue in the axial images of the 3D printed mouse phantom against the calculated contrast to noise ratios between the structure that represented soft tissue and bone in each axial images of the 3D printed mouse phantom for the different pre-filters. From figure 4.1 it is observed that:

1. The G3 $\times$ 3 pre-filter results in the lowest SNR_{st} and CNR_{bs}.
2. The EPIT10 pre-filter offers the highest SNR_{st} and CNR_{bs}.
3. The SNR_{st} and CNR_{bs} for the Gaussian low-pass and Median pre-filter increase with increasing kernel size.
4. SNR_{st} and CNR_{bs} for the edge-preserving pre-filter increase with increasing number of iterations.

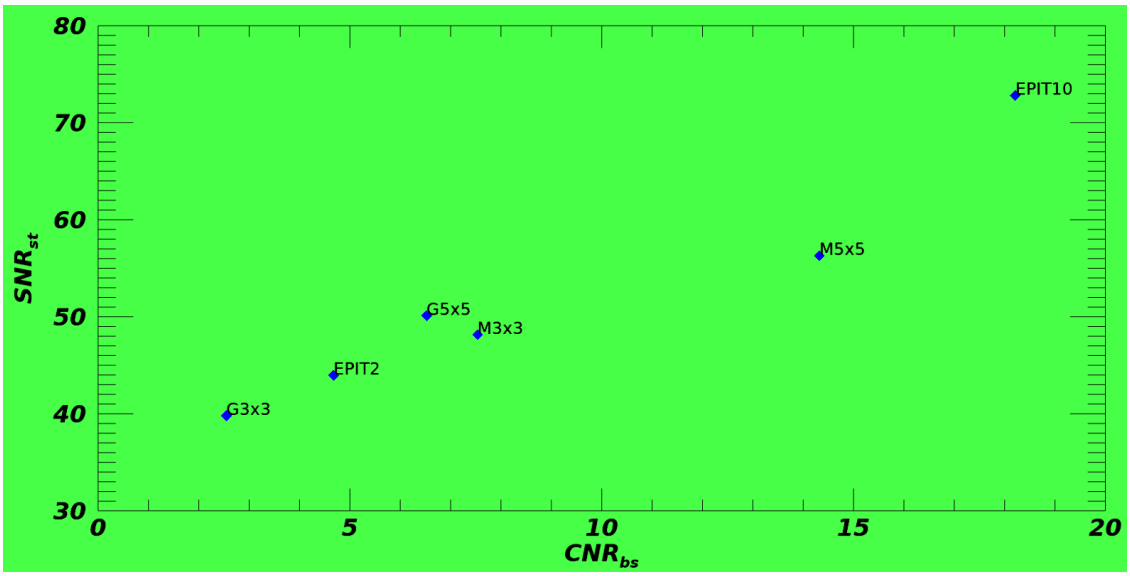

Figure 4.1: *Calculated* SNR_{st} *against* CNR_{bs} *for the different pre-filters.*

4.2 External corrections

Figure 4.2 shows two axial images of the 3D printed mouse phantom that were extracted from the CBCT images of the 3D printed mouse phantom, One which was reconstructed with external corrections, and the other without external corrections. From figure 4.2a it is observed that the image of the that was reconstructed without external corrections contains several ring artefacts. On other hand, no ring artefacts are observed in the image that was reconstructed with external corrections as shown in figure 4.2b. Note that the ring artefacts were not removed completely from CBCT image with external corrections.

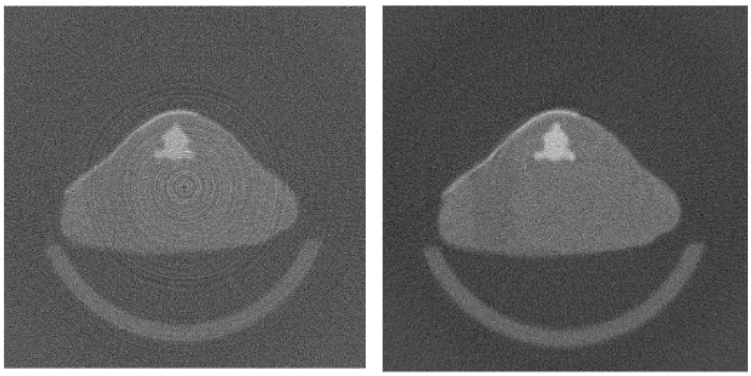

(a) (b)

Figure 4.2: *Demonstration of external corrections. An axial image of the 3D printed mouse phantom which was reconstructed without external corrections (a), and with external corrections (b).*

4.2.1 CBCT image reconstruction protocol in MuriSlice

Table 4.2 shows the created CBCT image reconstruction protocol in Murislice which contains reconstruction parameters that were selected based on the optimisation criterion described in section 3.4.

Table 4.2: *CBCT image reconstruction protocol in Murislice.*

Voxel size	$(100\,\mu m)^3$
Reconstruction algorithm	FDK algorithm
Reconstruction filter	Hamming filter
pre-filter	EPIT10

4.3 Comparison of μRayStation 8B dose calculations

Figure 4.3 presents two μRayStation 8B calculated percentage depth dose curves (PDD) for Phantom 1. The first (figure 4.3 orange PDD curve) was obtained by assigning material and mass density using the CBCT Hounsfield unit to mass density calibration, and the second (figure 4.3 cyan PDD curve) was obtained by assigning material and mass mass density based on manual identification. Figure 4.3 shows that both PDD curves decrease with increasing depth, however, large fluctuations are observed in the PDD curve that was obtained using the Hounsfield unit to mass density calibration. On the other hand, the fluctuations in the PDD curve that was obtained using manual identification are below 1 %.

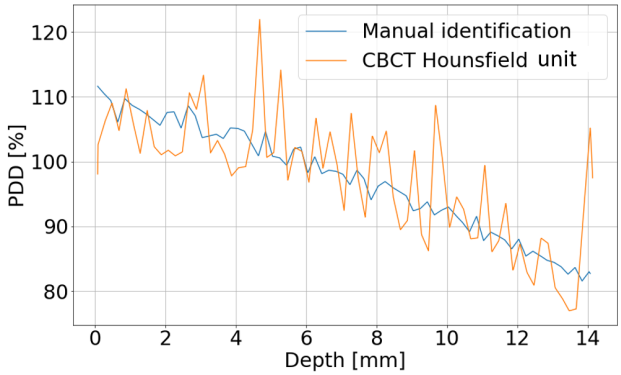

Figure 4.3: *μRayStation 8B calculated percentage depth dose curves for Phantom 1.*

4.4 Comparison of PDD between film measurements and μRayStation 8B dose calculations

Figure 4.4 presents μRayStation 8B calculated PDD curves and EBT3 film measured PDD points. The curves were all obtained from μRayStation 8B dose calculations performed on CBCT images of the four slab phantoms which were assigned material and mass density based on manual identification. It is observed that the measured points and calculated curves are in reasonable agreement. Figure 4.4a shows that the calculated curves and the measured points for Phantom 1 decrease with increasing depth in Phantom 1. The calculated curves and measured points for the remaining phantoms vary over different depth ranges as seen in figure 4.4b, 4.4b, and 4.4d.

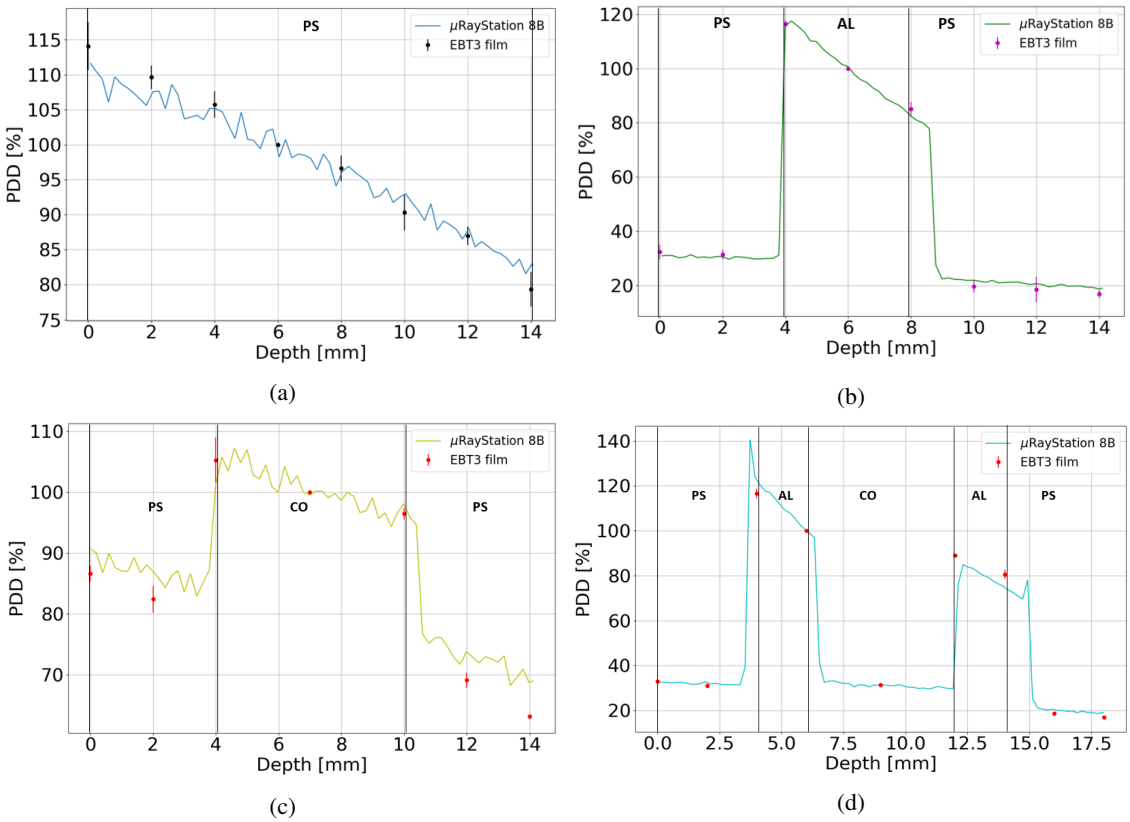

Figure 4.4: *Measured PDD and μRayStation 8B calculated PDD curves for phantom 1 (a), Phantom 2 (b), phantom 3 (c), and phantom 4 (d). The bars represents standard deviations in the measured PDD.*

Table 4.3 shows the mean deviations Δ_{mean} between the PDD curve values calculated by the μRayStation 8B and the PDD points measured by the EBT3 films for the four slab phantoms. In the same table the maximum deviations Δ_{maximum} between the curve values and measured points are also presented. From table 4.3, an increase in the Δ_{mean} and Δ_{maximum} values can be observed as the complexity in the heterogeneity of the phantom increases. From table 4.3 it is observed that the Δ_{mean} and Δ_{maximum} values are lowest for Phantom 1 and highest for Phantom 4.

Table 4.3: Δ_{mean} *and* Δ_{maximum} *for the four slab phantoms.*

Phantom	Δ_{mean} [%]	Δ_{maximum} [%]
1	0.4	2.4
2	1.6	2.9
3	3.5	4.2
4	4.6	12

Chapter 5

Discussion

5.1 CBCT image reconstruction protocol in MuriSlice

The primary aim of this thesis was to optimise the CBCT image reconstruction protocol in MuriSlice by optimising two selected parameters to enable segmentation of CBCT images of the objects generated by Murislice in μRayStation 8B. The two parameters of the CBCT image reconstruction protocol in MuriSlice that were selected and optimised were the voxel size and the pre-filter settings. The optimised image reconstruction protocol is presented in table 4.2. The optimisation criteria were:

1. to reduce as many ring artefacts and as much noise as possible from the reconstructed CBCT images.
2. to obtain as high a spatial resolution as possible in the reconstructed CBCT images.
3. to obtain as high a contrast resolution as possible between the different structures in the reconstructed CBCT images.

The calculated SNR of the axial images of the water phantom increases when the voxel size increases from (100 μm)^3 to (200 μm)^3, and then decreases when the voxel size increases from (200 μm)^3 to (300 μm)^3 as seen in table 4.1. The SNR is expected to increase with increasing voxel size because the value of the attenuation coefficient in that voxel is the average of the values of the attenuation coefficients within the large voxel. The observed decrease in SNR between (200μm)^3 and (300μm)^3 may be a result of ring artefacts in the axial images of the cylindrical water phantom. However, this result requires further examination in future work. The voxel size also affects the resolution of the image because the smaller the voxel the better the resolution. However, Verhagen *et al* recommends a voxel size of at least (130 μm)^3 for small animal imaging [3]. A voxel size of (100μm)^3 was selected as a trade-off between the spatial resolution and the calculated SNR of the axial CBCT images of the water phantom for the purpose of this thesis, and it is noted that this value is not far from the recommendation by Verhagen et al.

The EPIT10 pre-filter was selected because it offers the highest CNR_{bs} and SNR_s in the axial CBCT images of the 3D printed mouse phantom as observed in figure 4.1.

The reconstruction protocol in MuriSlice was also tested through the reconstruction of the images of the four slab phantoms and the subsequent segmentation of these CBCT images in μRayStation 8B. The images of the four slab phantoms were successfully segmented in the μRayStation 8B because the CNR between the studied structures in these images was sufficient to differentiate these structures. The primary aim was successfully achieved because the images of the four slab phantoms were segmented in μRayStation 8B.

5.2 Comparison of PDD between film measurements and μRayStation 8B dose calculations

The secondary aim of this thesis was to verify the MC dose calculation algorithm in μRayStation 8B that is used for dose calculation on the CBCT images by comparison with ETB3 film measurements.

Before comparing the μRayStation 8B calculated PDD curves of the different slab phantoms, the following two methods were used to determine the type of material present in the voxels of the CBCT image of Phantom 1:

1. CBCT Hounsfield unit to mass density calibration.
2. Manual identification and delineation.

The resulting PDD curves obtained using these two methods are presented in figure 4.3. The large fluctuations, observed in the orange PDD curve (see figure 4.3) calculated based on the CBCT Hounsfield unit to mass density calibration, depend on the noise present in the CBCT image of Phantom 1. In section 3.10, it was explained that in order to perform dose calculation, μRayStation 8B assigns material to each voxel of the CBCT image using its mass density that was obtained through the CBCT Hounsfield unit to mass density calibration. The VMC++ dose algorithm in μRayStation 8B uses the information about the voxel material to select cross-section data for the dose calculation. The large fluctuations in the CBCT image of Phantom 1 cause the large fluctuations in the calculated PDD curve. On the other hand, when the material is assigned to the CBCT image of Phantom 1 based on manual identification, the fluctuations in the cyan PDD curve (in figure 4.3) are below 1 %. The manual identification method in μRayStation 8B overrides the Hounsfield calibrated mass density assigned to the CBCT image by allowing the user to define the mass density used to select materials and subsequently select the cross-section data for dose calculation. The problem posed by the noise in the CBCT image of Phantom 1 is bypassed by assigning materials to its voxels based on manual identification because of the proper selection of cross-section data during dose calculation. Therefore, the fluctuations in the μRayStation 8B calculated PDD curve are below 1%. For accurate dose calculation, it is necessary to reduce as much noise as possible from the CBCT images.

By looking at figure 4.4 reasonable agreement is observed between the measured PDD points and calculated PDD curves for the four slab phantoms. The decrease in PDD observed as the depth in Phantom 1 increase (see figure 4.4a) is expected because the phantom was homogeneous, consisting only of polystyrene, denoted as PS. The differences in PDD as depth increases that are observed for the remaining phantoms are a result of the heterogeneity in the material of the phantoms. Note that Phantoms 2-4 consisted of different combinations of polystyrene, aluminium, and cork. This is consistent with the findings for Phantom 1 as the PDD was dependent on the material present at the depth of the phantom.

The observed increase of the Δ_{mean} and Δ_{maximum} values as the heterogeneity in the four slab phantoms increases in complexity indicates that the VMC++ dose calculation algorithm in μRayStation 8B calculates the dose for homogeneous materials more accurately than for heterogeneous materials. This conclusion confirms the importance of assigning the right materials to the voxels of the CBCT image of the object to obtain more accurate dose calculations with the VMC++ dose calculation algorithm in μRayStation 8B.

5.3 Future prospects

The results obtained in this thesis will allow for the testing of the current CBCT reconstruction protocol in MuriSlice to be applied to small animals, and further test if these images can be segmented in μRayStation 8B. Using the results from this thesis as a foundation, dose calculations can be more precise by using segmentation, but this can only happen if the noise and artefacts are reduced or eliminated from the CBCT images. This thesis gives the opportunity for future research to refine the current protocol in MuriSlice by optimising other reconstruction parameters such as the reconstruction filter and post-filters.

Chapter 6

Conclusion

An optimised image reconstruction protocol for the XenX's built-in CBCT has been developed in MuriSlice. This protocol enables the reconstruction of CBCT images with reduced noise and a minimal number of ring artefacts. The CBCT images of phantoms which are generated with this protocol can be segmented in μRayStation 8B. Future work is required to optimise additional reconstruction parameters for further noise reduction and less fluctuation to allow for more accurate dose calculations for external beam radiotherapy of small animals based on the CBCT images acquired with XenX.

Appendix A

Specifications of the XenX's X-ray tube

The specifications for the X-ray tube of the XenX are presented in table A.1 .

Table A.1: *Specification of the X-ray tube.*

Voltage range [kV]	20-220
Maximum current [mA]	13
Target material	Tungsten
Target angle [°]	20
Filter material	Copper, Aluminium
Thickness of copper filter [mm]	0.5
Thickness of aluminium filter [mm]	1.5

Appendix B

Specifications of the digital camera in the XenX's CBCT imaging system

The specifications for digital camera in the XenX's CBCT imaging system are presented in table B.1.

Table B.1: *Specifications of the digital camera.*

Sensor area (Height × Width)	113 mm × 70 mm
Sensor matrix (Height × Width)	1920 × 1200 pixels
Pixel type	Isotropic
Pixel Area	58.6 μm × 58.6 μm
Readout rate (Frame rate)	50 fps
Quantum efficiency	70 %
Dark noise	6.7 electrons
Pixel bit depth	8

Appendix C

Correction for Barrel distortion

In this section, the calibration part and the correction part of the correction for Barrel distortion in the are explained. The calibration part included the following steps:

1. A cone-beam X-ray projection of the metallic grid of holes was acquired with the XenX's CBCT imaging system which operated at a tube voltage of 60 kV and tube current of 0.8 mA.

2. The cone-beam X-ray projection of the metallic grid of holes was segmented by using the thresholding segmentation method [35, 36].

3. The coordinates of the centre of each holes in the segmented cone-beam X-ray projection of the metallic grid of holes were fitted to horizontal parabolas ($y(x)_i$) and vertical parabolas ($x(y)_j$) given by [36]:

$$y(x)_i = A_i x^2 + B_i x + C_i, \text{ for } i \in \{1, ..., N\} \tag{C.1}$$

$$x(y)_j = A_j y^2 + B_j y + C_j, \text{ for } j \in \{1, ..., M\}. \tag{C.2}$$

   Where:

   - i: denotes the index for ith the horizontal parabola.
   - j: denotes the index for the jth vertical parabola.
   - A_i, B_i and C_i: denote the coefficients of the ith horizontal parabola.
   - A_j, B_j and C_j: denote the coefficients of the jth vertical parabola.
   - N: denotes the total number of horizontal parabolas.
   - M: denotes the total number of vertical parabolas.

3 . The coordinates of the centre of the Barrel distortion COD (x_{COD},y_{COD}) were estimated in the following manner [35, 36]:

   (a) The two adjacent horizontal and vertical parabolas with opposite A coefficients were determined amongst the vertical and horizontal parabolas.

   (b) The coordinates for the COD (x_{COD}, y_{COD}) were estimated as the average of the C coefficients of these horizontal and vertical parabolas.

4 . Next, the coefficients for a polynomial model for the Barrel distortion were estimated. In this model the coordinates of the hole (x_u, y_u) in the Barrel undistorted cone-beam X-ray projection of the metallic grid of holes and the corresponding hole (x_d, y_d) in the Barrel distorted cone-beam X-ray projection the metallic grid of holes are related through the following expression [36],

$$F(r_u) \equiv r_d = r_u \left(\sum_{n=0}^{L} k_n r_u^n \right), \tag{C.3}$$

where:

- L: denotes the order of the polynomial model.
- r_d: denotes the distance from (x_d, y_d) to the COD in the Barrel distorted cone-beam X-ray projection of the metallic grid of holes.
- r_u: denotes the distance from (x_u, y_u) to the COD in the Barrel undistorted cone-beam X-ray projection of the metallic grid of holes.
- k_n: denotes the distortion coefficients of the polynomial model.

The coefficients (k_n) for the polynomial model in Eq. C.3 were calculated by solving the following linear system of equations using least square method for each hole on the horizontal and vertical parabolas [36],

$$\begin{bmatrix} 1 & \frac{r_d}{F_i} & \cdots & \frac{r_d^n}{F_{i,n}} \\ \vdots & \vdots & \cdots & \vdots \\ 1 & \frac{r_d}{F_j} & \cdots & \frac{r_d^n}{F_{j,n}} \\ \vdots & \vdots & \cdots & \vdots \end{bmatrix} \begin{bmatrix} k_0 \\ k_1 \\ \vdots \\ \vdots \\ k_n \end{bmatrix} = \begin{bmatrix} F_i \\ \vdots \\ F_j \\ \vdots \end{bmatrix}. \tag{C.4}$$

Where:

- $F_j = \frac{A_j x^2 + C_{j,d}}{C_{j,u}}$, where $C_{j,u}$ is the intersection between the y-axis and the jth vertical parabola in the segmented cone-beam X-ray projection of the grid of holes and was determined by extrapolating from a few lines close to the COD in the cone-beam X-ray projection of the metallic grid of holes [36],

$$C_{j,u} = \left(\operatorname{sgn}(C_j) \times |(j - j_0) \times \overline{\Delta C_h}| \right) + C_{j_0}. \tag{C.5}$$

  Where:

  - j_0: denotes the index of the closest vertical line of the COD in the cone-beam X-ray projection of the metallic grid of holes.
  - $\overline{\Delta C_v}$: denotes the average difference of a few vertical lines close to the COD in the Barrel undistorted cone-beam X-ray projection of the metallic grid of holes.

- $F_i = \frac{A_i x^2 + C_{i,d}}{C_{i,u}}$, where $C_{i,u}$ was determined the same way as for the case of the horizontal lines but using vertical lines instead.

In this thesis, the linear equation system in equation Eq. refeq:lin was solved for a polynomial model of the Barrel distortion of second-order ($L = 1$) because as mentioned in Asari *et al.* [34] there is no gain in accuracy by using higher-order polynomial models.

The correction part involved the correction for Barrel distortion in the cone-beam X-ray projections. Below correction for the Barrel distortion in cone-beam X-ray projections of the 3D printed mouse phantom is presented. The same procedure was used to correct the Barrel distortion in cone-beam flat field X-ray projections. The Barrel distorted and Barrel undistorted cone-beam X-ray projections of 3D printed mouse phantom were treated as a grid of holes [36]. It is worth mentioning that the coordinate system for the cone-beam X-ray projections of the 3D printed mouse phantom and the fitted horizontal and vertical lines differs as explained in [36]. Because it is necessary to know these coordinate systems to understand how the correction works the reader is therefore referred to [36] for more details. The correction for a Barrel distorted cone-beam X-ray projection of the 3D printed mouse phantom involved the following steps [36],

1. The coordinates of a hole in undistorted cone-beam X-ray projection of 3D printed mouse phantom was translated,

$$\begin{bmatrix} x_u \\ y_u \end{bmatrix} = \begin{bmatrix} x_u - x_{COD} \\ y_u - y_{COD} \end{bmatrix} \tag{C.6}$$

2. The coordinates of the corresponding hole in the Barrel distorted cone-beam of X-ray projection (x_d, y_d) was determined,

$$\begin{bmatrix} x_d \\ y_d \end{bmatrix} = \frac{r_d}{r_u} \times \begin{bmatrix} x_u \\ y_u \end{bmatrix} \tag{C.7}$$

   where:

   - $r_u = \sqrt{x_u^2 + y_u^2}$
   - $r_d = r_u(k_0 + k_1)$, where k_0 and k_1 are the coefficients of second order polynomial model for the Barrel distortion.

3. The calculated coordinates of the hole in Barrel distorted cone-beam X-ray projection of were translated as,

$$\begin{bmatrix} x_d \\ y_d \end{bmatrix} = \begin{bmatrix} x_d + x_{COD} \\ y_d + y_{COD} \end{bmatrix} \tag{C.8}$$

4. Next, the four closest holes to (x_d, y_d) in the distorted cone-beam X-ray projection were determined as,

$$\begin{bmatrix} \lfloor x_d \rfloor & \lceil x_d \rceil \\ \lfloor y_d \rfloor & \lceil y_d \rceil \end{bmatrix} \tag{C.9}$$

   where:

   - $\lfloor \rfloor$: denotes the floor function which computed the greatest integer less or equal to its argument.
   - $\lceil \rceil$: denotes the ceil function which computes the integer greater or equal to its argument.

5. Finally, the pixel value at (x_d, y_d) was estimated by interpolating the pixel values at the 4 closest holes by using bilinear interpolation and the resulting pixel value was assigned to be (x_u, y_u) in the undistorted cone-beam X-ray projection of the 3D printed mouse phantom.

Appendix D

Normalised X-ray photon fluence spectra for the XenX's treatment beam

The normalised X-ray photon fluence spectra for the XenX treatment beam is presented in figure D.1.

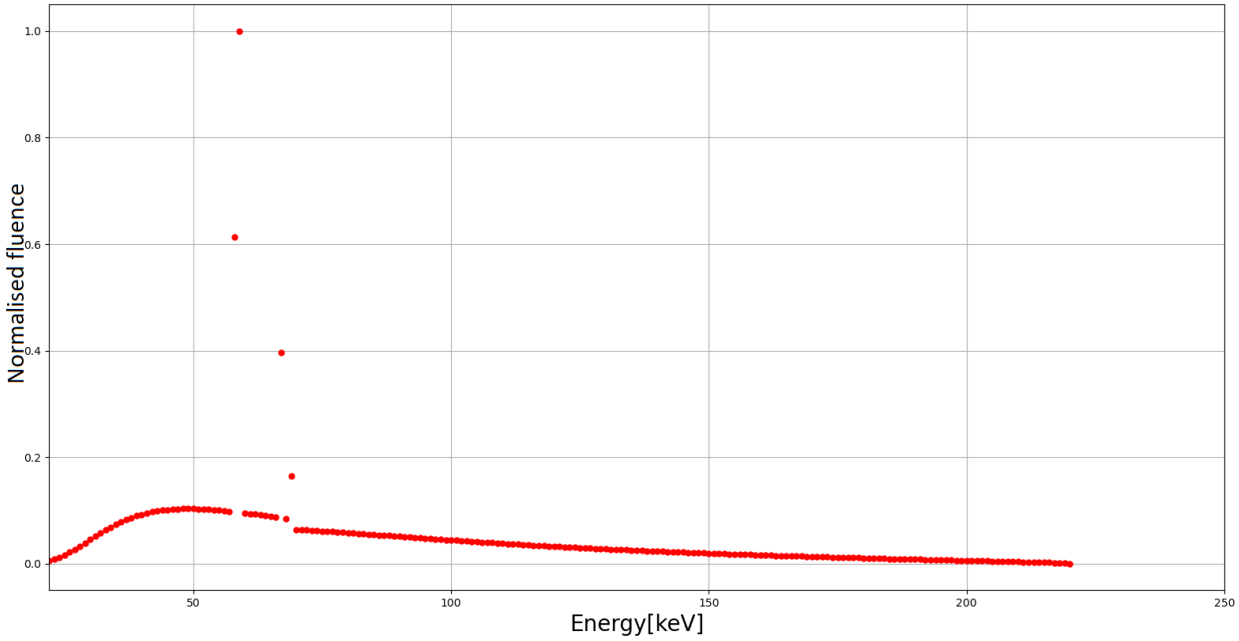

Figure D.1: *Normalised X-ray photon fluence spectra for the XenX's 220 kV beam of X-ray photons.*

References

[1] Podgorsak EB. Radiation physics for medical physicists. 3rd ed. Montreal: Springer; 2016.

[2] International WCRF. Global cancer data by country [internet]. World Cancer Research Fund International; No year [updated March 2022; cited 2022 Jul 14]. Available from: https://www.wcrf.org/cancer-trends/global-cancer-data-by-country/.

[3] Verhaegen F, Granton P, Tryggestad E. Small animal radiotherapy research platforms. Phys Med Biol. 2011 May 26;56(12):R55-83. Available from: https://iopscience.iop.org/article/10.1088/0031-9155/56/12/R01/meta.

[4] Maqbool M. An introduction to medical physics. Birmingham: Springer; 2017.

[5] Koontz BF, Verhaegen F, De Ruysscher D. Tumour and normal tissue radiobiology in mouse models: how close are mice to mini-humans? Br J Radiol. 2016 Jan 26;90(1069):20160441. Available from: https://www.birpublications.org/doi/full/10.1259/bjr.20160441.

[6] Chakwizira A, Ahlstedt J, Nittby Redebrandt H, Ceberg C. Mathematical modelling of the synergistic combination of radiotherapy and indoleamine-2, 3-dioxygenase (IDO) inhibitory immunotherapy against glioblastoma. Br J Radiol. 2018 May 17;91(1087):20170857. Available from: https://www.birpublications.org/doi/full/10.1259/bjr.20170857.

[7] Cai W. Engineering in translational medicine. London: Springer; 2014.

[8] Chiavassa S, Nilsson R, Clément-Colmou K, Potiron V, Delpon G, Traneus E. Validation of the analytical irradiator model and Monte Carlo dose engine in the small animal irradiation treatment planning system μ-RayStation 8B. Phys Med Biol. 2020 Jan 24;65(3):035006. Available from: https://iopscience.iop.org/article/10.1088/1361-6560/ab6155/meta.

[9] Verhaegen F, Hoof SV, Granton PV, Trani D. A review of treatment planning for precision image-guided photon beam pre-clinical animal radiation studies. Z Med Phys. 2014 Feb;24(4):323-34. Available from: https://www.sciencedirect.com/science/article/pii/S0939388914000312.

[10] Noblet C, Chiavassa S, Smekens F, Sarrut D, Passal V, Suhard J, et al. Validation of fast Monte Carlo dose calculation in small animal radiotherapy with EBT3 radiochromic films. Phys Med Biol. 2016 Apr 16;61(9):3521. Available from: https://iopscience.iop.org/article/10.1088/0031-9155/61/9/3521/meta.

[11] Knoll GF. Radiation detection and measurement. 4th ed. No place: John Wiley & Sons; 2016.

[12] Krane KS, Halliday D. Introductory nuclear physics. New York: John Wiley & Sons; 1988.

[13] Dance D, Christofides S, Maidment A, McLean I, Ng K. Diagnostic radiology physics: A handbook for teachers and students. Vienna: International Atomic Energy Agency; 2014.

[14] Ahmed SN. Physics and engineering of radiation detection. Amsterdam: Elsevier; 2007.

[15] Daniel R. Computational and experimental methods for imaging and dosimetry in ^{177}Lu radionuclide therapy [Dissertation]. Lund:Lund University; 2020.

[16] Grupen C, Buvat I. Handbook of particle detection and imaging. Berlin: Springer; 2011.

[17] Shaw CC. Cone beam computed tomography. Boca Raton: CRC Press,Taylor & Francis; 2014.

[18] Buzug TM. Computed tomography: From Photon Statistics to modern cone beam CT. Dordrecht: Springer; 2008.

[19] Kak AC, Slaney M. Principles of computerized tomographic imaging. New York: IEEE PRESS; 1988.

[20] Woods RE, Gonzalez RC. Digital Image Processing. 3rd ed. No place: Pearson education; 2008.

[21] Zeng GL. Medical image reconstruction: a conceptual tutorial. Heidelberg: Springer; 2010.

[22] Tsui B, Frey E. Analytic image reconstruction methods in emission computed tomography. In: Chapter 3, Quantitative analysis in nuclear medicine imaging. New York: Springer; 2006. p. 82-106.

[23] Feldkamp L, Davis LC, Kress JW. Practical cone-beam algorithm. J Opt Soc Am A. 1894;1(6):612-9.

[24] Curry TS, Dowdey JE, Murry RC. Christensen's Physics of diagnostic Radiobiology. 4th ed. Philadelphia: Lea & Febiger; 1990.

[25] Schulze R, Heil U, Groβ D, Bruellmann DD, Dranischnikow E, Schwanecke U, et al. Artefacts in CBCT: a review. DMFR. 2014 Jan 28;40(5):265-73. Available from: https://www.birpublications.org/doi/10.1259/dmfr/30642039.

[26] Verhaegen F, Dubois L, Gianolini S, Hill MA, Karger CP, Lauber K, et al. ESTRO ACROP: Technology for precision small animal radiotherapy research: Optimal use and challenges. Radiat Oncol. 2017 Dec 18;126(3):471-8. Available from: https://www.sciencedirect.com/science/article/pii/S0167814017327330.

[27] Reynaert N, Van der Marck S, Schaart D, van der Zee W, M T, Vliet-Vroegindeweij C, et al. Monte Carlo Treatment Planning—An Introduction. Report No 16. Netherlands: Netherlands Commission on Radiation Dosimetry; 2008.

[28] De Martino F, Clemente S, Graeff C, Palma G, Cella L. Dose Calculation Algorithms for External Radiation Therapy: An Overview for Practitioners. Appl Sci. 2021 Jul 21;11(15):6806. Available from: https://www.mdpi.com/2076-3417/11/15/6806.

[29] Seco J, Verhaegen F. Monte Carlo techniques in radiation therapy. Boca Raton: CPR press, Taylor & Francis; 2013.

[30] Biglin ER, Price GJ, Chadwick AL, Aitkenhead AH, Williams KJ, Kirkby KJ. Preclinical dosimetry: exploring the use of small animal phantoms. Radiat Oncol. 2019 Jul 31;14(1):1-10. Available from: https://ro-journal.biomedcentral.com/articles/10.1186/s13014-019-1343-8.

[31] Xstrahl. MuriSlice®Software Overview; No date.

[32] Xstrahl. Calibration File Description; 2014.

[33] Van Rossum G, Drake FL. Python 3 Reference Manual. Scotts Valley, CA: CreateSpace; 2009.

[34] Asari KV, Kumar S, Radhakrishnan D. A new approach for nonlinear distortion correction in endoscopic images based on least squares estimation. IEEE Trans Med Imaging. 1999 Apr;18(4):345-54.

[35] Vo NT, Atwood RC, Drakopoulos M. Radial lens distortion correction with sub-pixel accuracy for X-ray microtomography. Opt Express. 2015;23(25):32859-68.

[36] Vo NT. Python implementation of distortion correction methods for X-ray micro-tomography. Oxfordshike: Diamond Light source; 2015. 1-16.

[37] Raven C. Numerical removal of ring artifacts in microtomography. Rev Sci Instrum. 1998 Aug 03;69(8):2978-80.

[38] Nilsson M. μRayStation 8B User Guide Draft. RaySearch Laboratories. 2019.

[39] RaySearch. RAYSTATION 8B reference manual. RaySearch Laboratories. 2018.

[40] Fippel M. Monte carlo dose calculation for treatment planning. In: New technologies in radiation oncology. Springer; 2006. p. 197-206.

[41] Hubbell J, Seltzer S. X-Ray Mass Attenuation Coefficients [internet]. NIST; 1996 [updated Jul 1996; cited 2022 July 14]. Available from: https://www.nist.gov/pml/x-ray-mass-attenuation-coefficients.

[42] Fuse H, Fujisaki T, Ikeda R, Hakani Z. Applicability of Lung Equivalent Phantom Using the Cork with Absorbed Water in Radiotherapeutic Dosimetry. Med Phys Int. 2018 Feb 7;07(01):27-34. Available from: https://www.scirp.org/html/3-2660303_82321.htm.